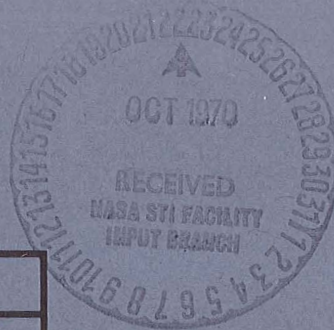


NASA CR-111776



IITRI

IIT Research Institute

IITRI Report V6098

ADVANCED EVALUATION OF VACUUM UV
DETECTOR-SPECTROSCOPY SYSTEMS
FOR CAPSULE REENTRY MEASUREMENTS

National Aeronautics & Space Administration
Langley Research Center
Hampton, Virginia 23365
NASA CR-111776

FACILITY FORM 602

N70-41918	
(ACCESSION NUMBER)	(THRU)
81	1
(PAGES)	(CODE)
QR-111776	26
(NASA CR OR TMX OR AD NUMBER)	(CATEGORY)

NASA CR-111776

IITRI Report V6098

ADVANCED EVALUATION OF VACUUM UV
DETECTOR-SPECTROSCOPY SYSTEMS
FOR CAPSULE REENTRY MEASUREMENTS

National Aeronautics & Space Administration
Langley Research Center
Hampton, Virginia 23365
NASA CR-111776

IIT RESEARCH INSTITUTE

NASA CR-111776

ADVANCED EVALUATION OF VACUUM UV
DETECTOR-SPECTROSCOPY SYSTEMS FOR
CAPSULE REENTRY MEASUREMENTS

by Ronald L. Ohlhaber,
Howard T. Betz, and
Earl H. Klugman

April 1970

Prepared under Contract No. NAS 1-8992 by
IIT Research Institute
Technology Center
Chicago, Illinois 60616

for

NATIONAL AERONAUTICS AND SPACE ADMINISTRATION

PREFACE

This technical report was prepared by IIT Research Institute, Chicago, Illinois 60616, for the National Aeronautics and Space Administration, Langley Research Center, on Contract No. NAS 1-8992. The program was under the direction of the Optics Research Section, Physics Division, IIT Research Institute, Project No. V6098.

Personnel who have contributed to this project include, H. T. Betz, J. S. Davis, E. H. Klugman, R. L. Ohlhaber and D. A. Pontarelli.

CONTENTS

	<u>Page</u>
SUMMARY	1
I. INTRODUCTION	1
II. REENTRY MEASUREMENT REQUIREMENTS	2
III. MEASURING SYSTEM FOR DETECTORS	8
A. Monochromator and Lamp	8
B. Detector Chamber	13
C. Detector Electronic System	17
IV DETECTORS	17
A. Nitric Oxide Ion Chamber	19
B. Sodium Salicylate Coated Photo-multiplier Tube	19
C. Fairchild FPM 200 Photodiode	20
D. Fairchild FPM 100 Phototransistor	20
E. United Detector Technology PIN-Spot/2 Photodiode	20
F. Hewlett Packard 5082-4204 PIN Photodiode	20
G. Stannic Oxide Crystals	23
H. University of Chicago Silicon Photodiode	23
V. MEASUREMENT ANALYSIS METHOD	25
VI MEASUREMENT RESULTS	26
A. Sensitivity and Minimum Detectable Power	27
B. Array Elements	34
C. Fatigue and Memory Effects	38
D. Temperature Effects	44
E. Long Term Stability	47
F. Frequency Response	47
G. Other Parameters	47
1. Reverse Bias Voltage	47
2. Spatial Resolution	48
VII NOISE CONSIDERATIONS	48
A. Noise Sources	48
1. Johnson or Thermal Noise	50
2. Generation-Recombination (g-r) Noise	50
3. Flicker or Modulation (1/f) Noise	51
4. Environmental Noise	52
5. Total Noise	52

PRECEDING PAGE BLANK NOT FILMED

B.	Noise Measurements	52
1.	Silicon Reversed-Bias Photo- diodes	52
2.	Johnson Noise	55
3.	G-R Noise and Dark Current	55
4.	Detector-Preamplifier Interface	55
5.	Noise Power Spectra	60
VIII	SPECTROMETER DESIGN	64
A.	Design I Ebert-Fastie Spectrometer	64
B.	Radiant Power	66
C.	Other Spectrometer Designs	69
IX	CONCLUSION	71
	REFERENCES	75

FIGURES

<u>Figure No.</u>		<u>Page</u>
1.	Spectral Flux at Body, Adiabatic Case	4
2.	Spectral Flux at Body, Nonadiabatic Case	5
3.	Spectral Intensity at Body, Adiabatic Case	6
4.	Spectral Intensity at Body, Nonadiabatic	7
5.	Schematic of Optical System with Seya- Namioka Spectrometer	9
6.	Design of Experimental Vacuum System	10
7.	Disassembled Aluminum Cathode and Quartz Capillary of the McPherson UV Lamp	11
8.	Differential Pumping Chamber Assembly	12
9.	Experimental System Components	14
10.	Rear View of Heater and Temperature Sensor Locations	15
11.	Detector Chamber with Connections to Rear Door	16
12.	Detector System Components	18
13.	Detector Elements	21
14.	Solid State Detector Connections	22
15.	University of Chicago Photodiode	24
16.	Helium Emission Spectrum Between 500 and 2000 Angstroms	28
17.	Helium Spectrum from the U of C Photodiode No. 1490 at 7V Reverse Bias	29
18.	Helium Spectrum from the UDT-2 Photodiode	30
19.	Spectral Quantum Efficiency for Various Detectors	31
20.	Spectral Sensitivity of Solid State Detectors	33

21.	Detector Scans Behind 0.25mm Wide Exit Slit with 584.3 Å Radiation	35
22.	Detector Scans Behind 0.25mm Wide Exit Slit with 1215.7 Å Radiation	36
23.	Detector Scans Behind 0.25mm Wide Exit Slit with 584.3 Å Radiation	37
24.	Fatigue Measurement on UDT-1-B for 1215.7Å Radiation	40
25.	Fatigue Measurements at Two Spots on the UDT-1-B Detector Element with 584.3 Å Radiation	41
26.	Fatigue Tests for 1215 Å Radiation	42
27.	Decline in Relative Quantum Efficiency of the Sodium Salicylate Coated PM Tube	43
28.	Reverse Current as a Function of Detector Temperature	45
29.	Noise Variation with Temperature in the UDT-1-B Photodiode	46
30.	Penetration of Radiation in Silicon	49
31.	Ideal Diode Noise Spectrum	53
32.	Equivalent Circuit of a Silicon Photodiode	54
33.	Input Circuit for Noise Measurement	57
34.	Noise Measurement System	61
35.	Measured Diode Noise Spectrum	63
36.	Design I Ebert Spectrometer for Vacuum UV	65
37.	Spectral Radiance of Body, Adiabatic Case	67
38.	Spectral Radiance of Body, Nonadiabatic Case	68

TABLES

<u>Table No.</u>		<u>Page</u>
1.	Measurement Requirements	3
2.	Detectors	19
3.	Noise Equivalent Power	34
4.	Detector Dark Current & G-R Noise	44
5.	Rated Frequency Response	47
6.	Reverse Bias Voltage Range	48
7.	Noise Measurement Parameters	59
8.	Noise Measurement Parameters	60
9.	Spectral Radiation at Detector Plan for Ebert Spectrometer Design I	69
10.	Expected Signal to Noise Ratio for the Detectors for the Design I Ebert Spectrometer	70

ADVANCED EVALUATION OF VACUUM UV DETECTOR-SPECTROSCOPY SYSTEMS FOR CAPSULE REENTRY MEASUREMENTS

By Ronald L. Ohlhaber,
Howard T. Betz, and
Earl H. Klugman

IIT Research Institute

SUMMARY

During this program measurements were made on various solid state detectors to predict their performance for incorporation into a vacuum ultraviolet spectrometer that would be on-board a spacecraft designed to reenter the earth atmosphere at a velocity of 50,000 feet per second. Solid state silicon surface barrier and diffused junction photodiodes, phototransistors, and stannic oxide crystals, as detector arrays or individual detectors which could be assembled into arrays were tested in a Seya-Namioka monochromator over the 500 to 2000 angstrom region to determine wavelength sensitivity and other operational characteristics. The detector noise-limited frequency response was established, and fatigue problems were found in all detectors but the phototransistors. The surface barrier array elements on a single silicon chip exhibited considerable crosstalk. An initial spectrometer design incorporating the results of the detector measurements was also considered.

I.

INTRODUCTION

This study was to determine the operational properties of various types of solid state detectors which could be employed in a vacuum ultraviolet spectrometer that will be on-board a spacecraft designed to reenter the earth atmosphere at a velocity of 40,000 to 60,000 feet per second. The general mission application is for vehicles returning from Mars or Venus. The detector system conceptually consists of a single unit or discrete element array that would be located in the exit plane of a spectrometer. Photodiodes, phototransistors, silicon surface barrier diodes, and stannic oxide crystals which were arrays or elements for combination into an array, were investigated to determine their performance in the 500 to 2000 angstrom wavelength region.

A vacuum ultraviolet monochromator was modified so that a number of the detectors could simultaneously be mounted under vacuum in a chamber and alternately be positioned into the radiation path at the monochromator exit plane. The detector performance for various spectral lines was then measured and the data applied to a preliminary spectrometer system design.

II. REENTRY MEASUREMENT REQUIREMENTS

A detailed presentation of the measurement requirements including capsule conditions, instrument requirements, flight conditions, and shock front radiation has been given in a previous report.¹ However, the general conditions are again reviewed in Table 1. Since the exact vehicle trajectory and size are presently unknown, variations in some parameters may occur.² The spectrometer system is presently oriented to viewing the radiation at the vehicle stagnation point through an orifice in the heat shield.

Since no solid window materials transmit radiation at wavelengths less than 1050 angstroms the preliminary design is to employ a helium window system wherein the cavity is over-pressured with helium during reentry. An initial³ study of such a system was performed by Slocumb and Buchan³ who found the best performance using a 4.75 mm (3/16 in.) diameter orifice. This diameter along with a 19 mm (3/4 in.) thick heat shield has been used in the spectrometer design calculations of a latter chapter.

Updated spectral energy distributions for a 48,000 feet per second lifting entry, adiabatic and nonadiabatic cases, received from NASA Langley Research Center are presented in Figures 1 through 4. This data remains in very close agreement with the radiative fluxes previously presented in reference 1.

TABLE 1. MEASUREMENT REQUIREMENTS

FLIGHT CONDITIONS

Reentry Velocity:	40,000 to 60,000 ft/sec.
Reentry Altitude:	starts at 40,000 ft.
Maximum Acceleration:	60g
Stress Conditions:	1. thermal, heat transfer 2. g-stress, deceleration 3. vibrational 4. acoustical
Heat Pulse Duration:	80 sec.

CAPSULE CONDITIONS

Forebody Orifice Diameter:	4.75 mm (3/16 in.)
Heat Shield Thickness:	19 mm (3/4 in.)
Helium Window	
Instrument Cavity	

INSTRUMENT REQUIREMENTS

Spectral Coverage:	500 to 20,000 angstroms
UV Spectrometer:	500 to 2,000 angstroms
Resolution:	50 angstrom elements
Scan Rate:	5 sec. or less
Intensity Range:	50 watts/50 Å element

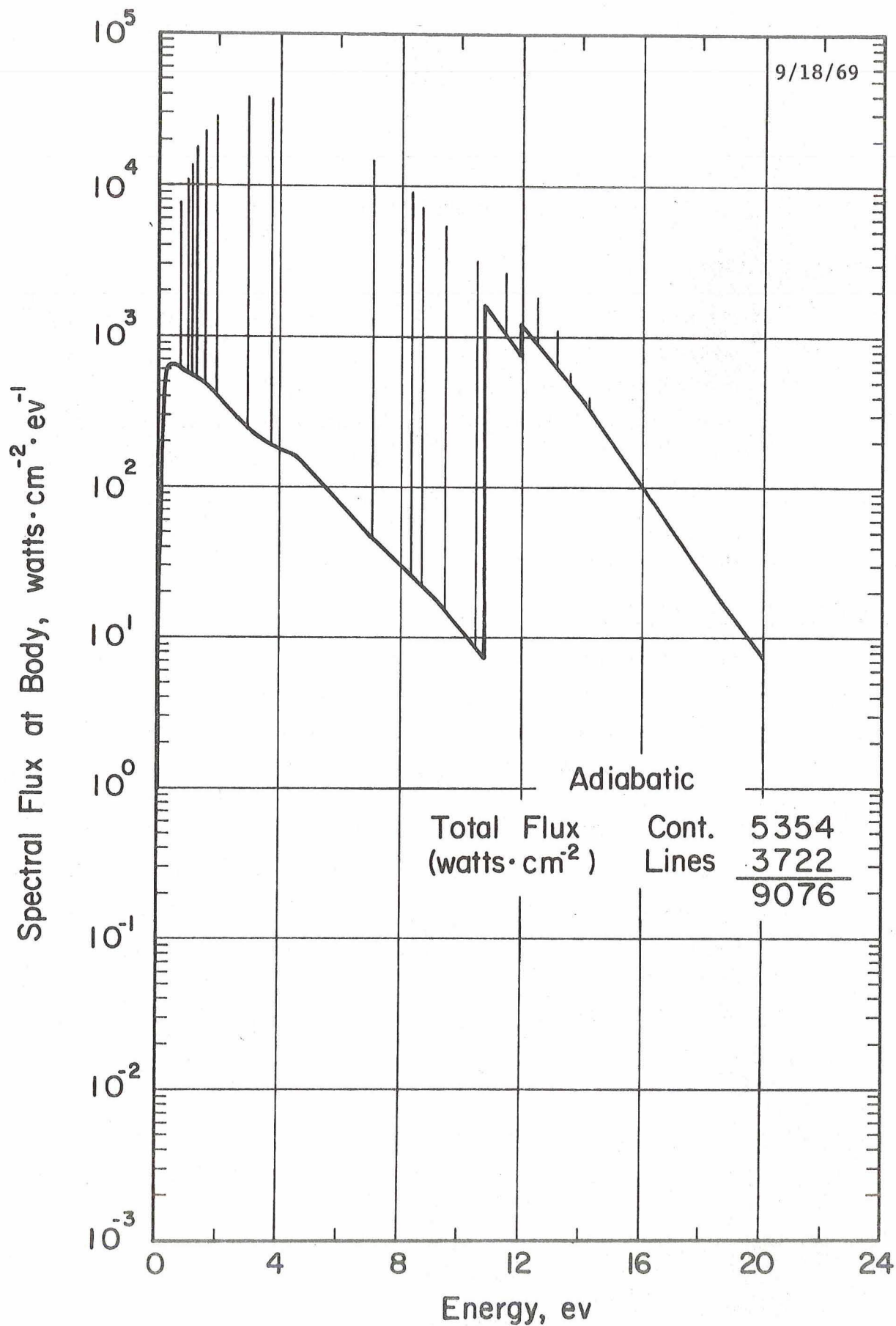


FIGURE 1. SPECTRAL FLUX AT BODY, ADIABATIC CASE

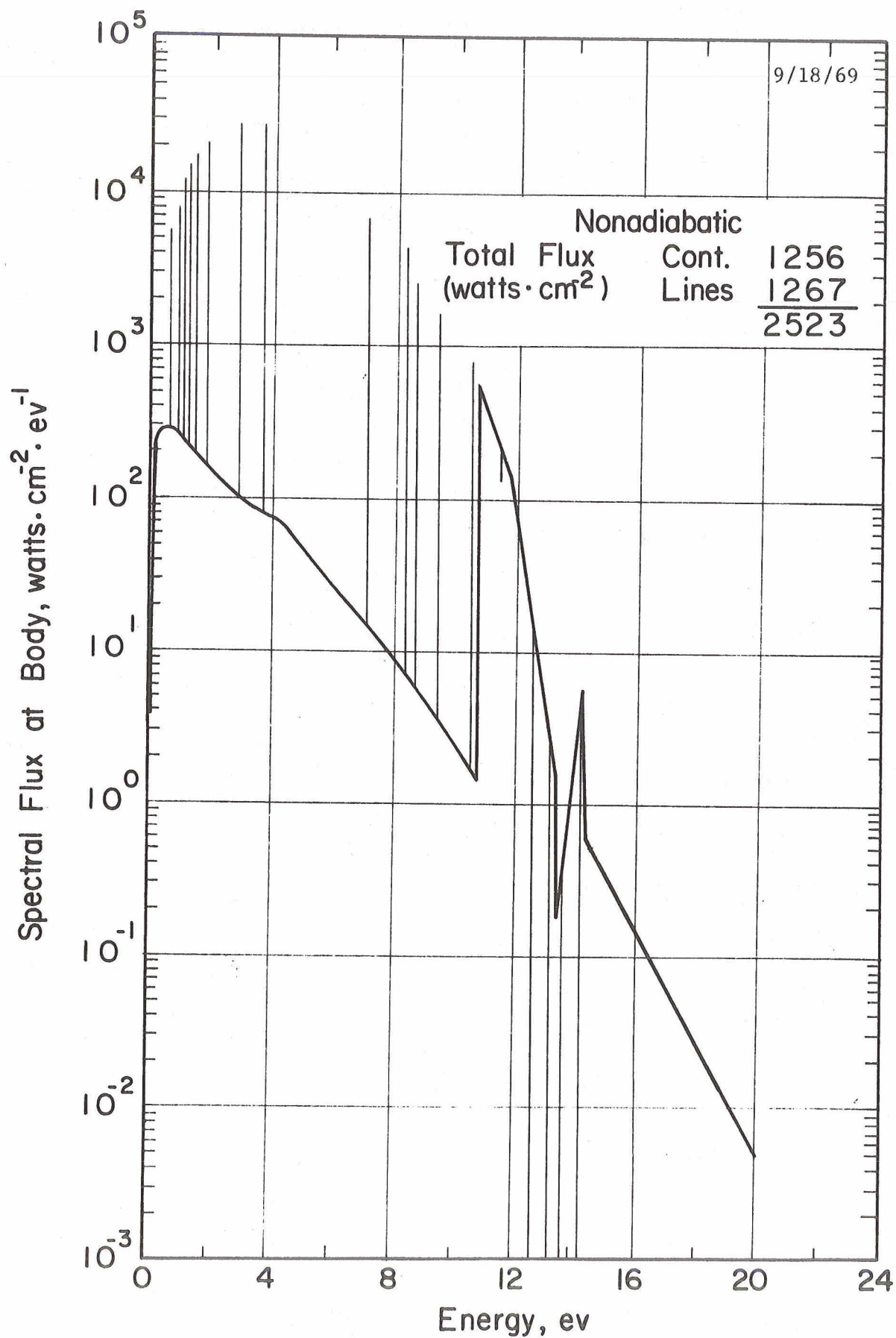


FIGURE 2. SPECTRAL FLUX AT BODY, NONADIABATIC CASE

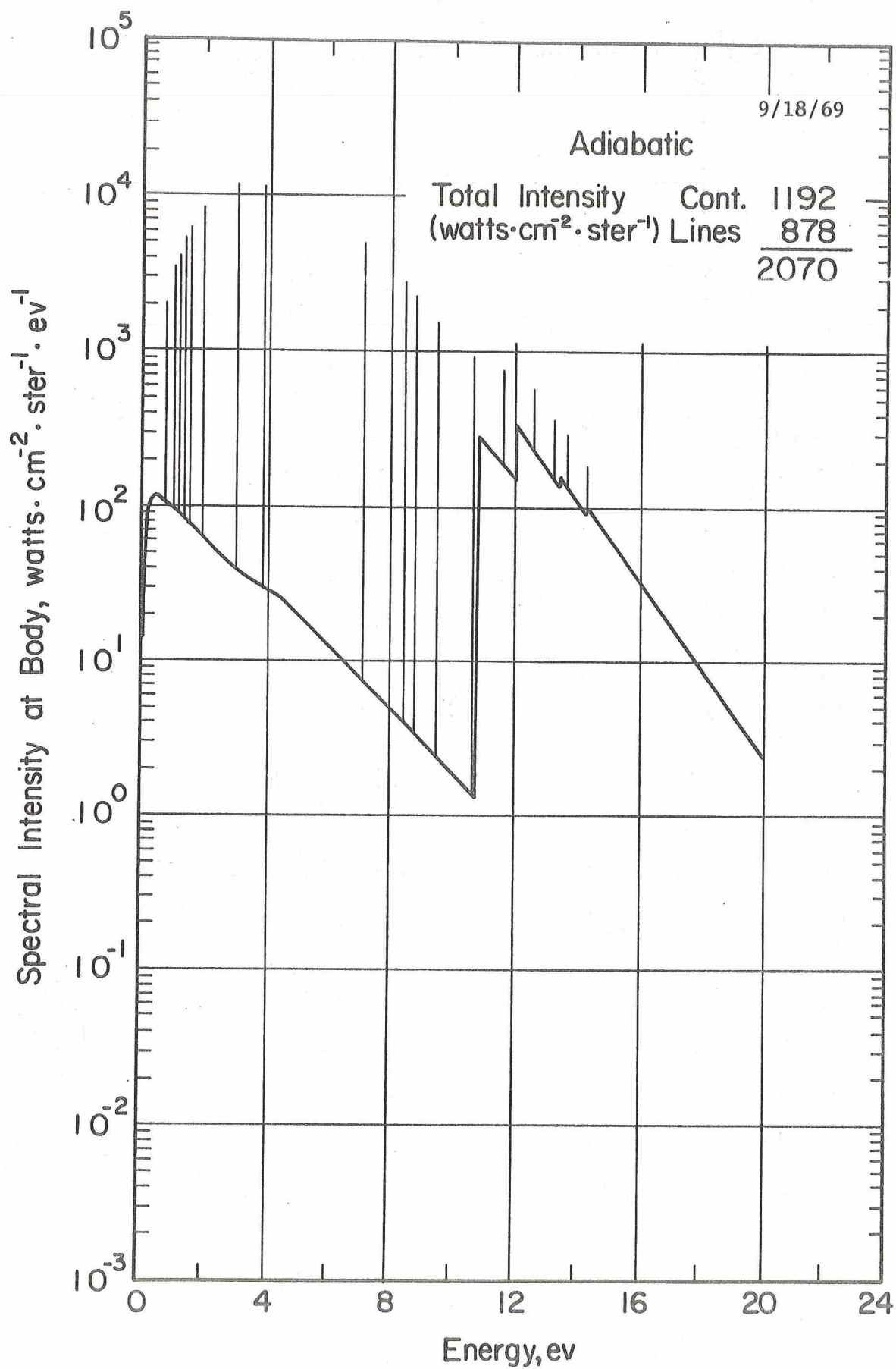


FIGURE 3. SPECTRAL INTENSITY AT BODY, ADIABATIC CASE

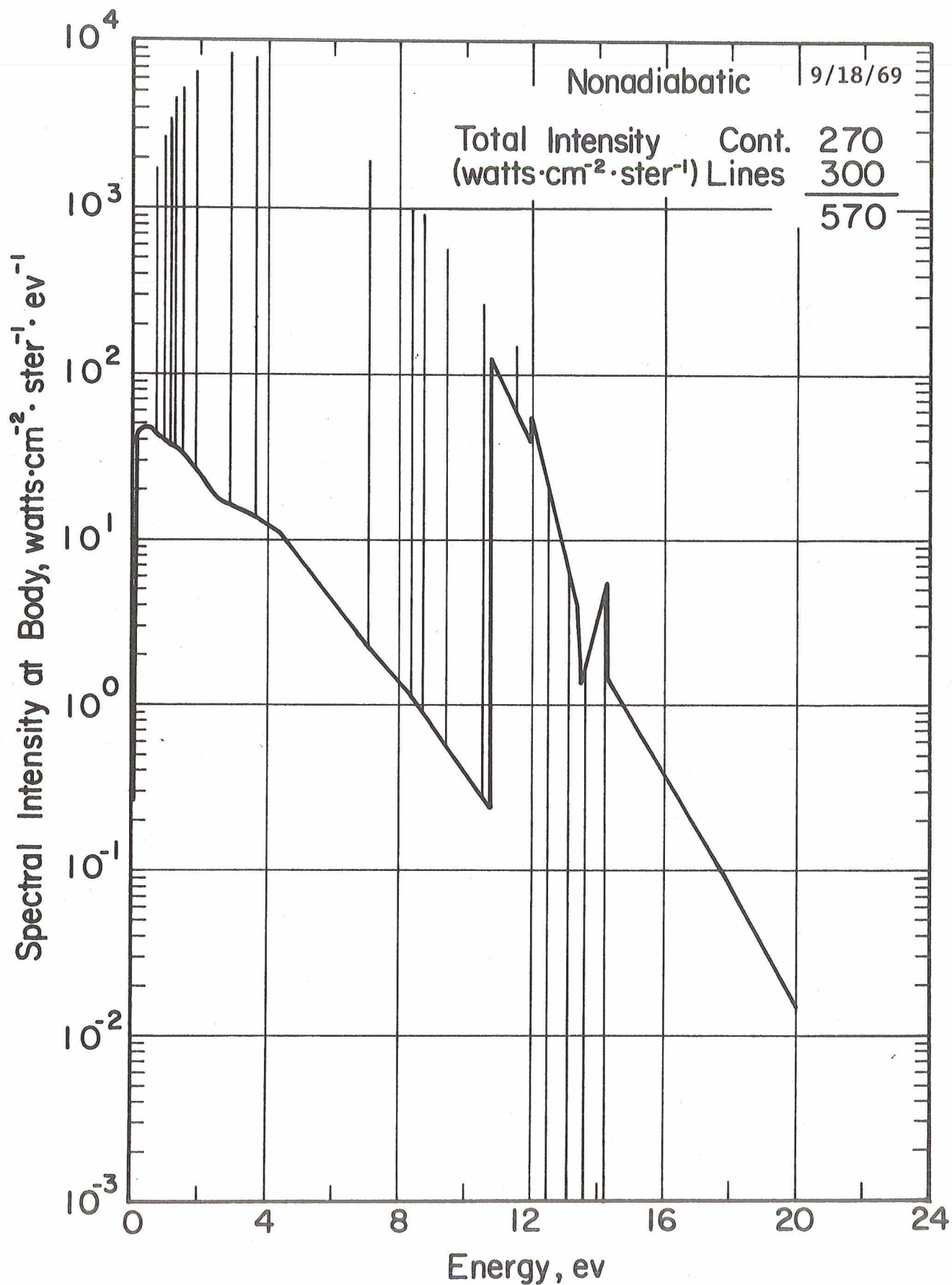


FIGURE 4. SPECTRAL INTENSITY AT BODY, NONADIABATIC CASE

III.

MEASURING SYSTEM FOR DETECTORS

A Seya-Namioka half-meter monochromator with a⁴⁻⁵ McPherson Model 630 Hinteregger-type discharge lamp generated the desired vacuum ultraviolet radiation. The photon beam upon leaving the monochromator was modulated by a vibrating blade chopper and passed through an exit slit to strike the detector which was positioned by a moveable plate controlled from outside the vacuum chamber. The complete optical system is shown in Figure 5. The detector signals were synchronously detected with a lock-in-voltmeter and the output displayed on a chart recorder.

A. Monochromator and Lamp

The monochromator contained a 4.5 x 3 cm reflection grating which was used in the first order. The grating could be set at a single position or scanned at a desired speed over a spectrum region. Initial measurements with a sodium salicylate coated photomultiplier tube showed that spectrum lines between 584 and 4500 angstroms could be accurately measured. The monochromator vacuum system consisted of a cold trap, diffusion pump and mechanical pump. Additional pumping was provided with two other complete vacuum systems shown in Figure 6. This permitted operation of the main monochromator chamber at pressures of approximately 4×10^{-5} Torr.

The McPherson lamp consists of a water cooled anode operated at ground potential and a hemispherical cathode connected by a water cooled quartz capillary tube in which the plasma forms. Initial operation with the air cooled cathode resulted in periodic servicing of the "O" ring sealing the cathode to the capillary tube due to the burning of the "O" ring. The removed cathode and the burnt deposits on the capillary assembly can be seen in Figure 7. Later to reduce lamp failure the cathode was water cooled. During this study the lamp was supplied with helium, hydrogen, or argon gas, or a mixture thereof. Normal operation was at gas line pressures below 1 Torr and differential pumping system pressures between 3 and 8×10^{-4} Torr. The input pressure was adjusted with a needle valve to less than one Torr absolute pressure. The system was operated windowless for all measurements.

A differential pumping chamber, Figure 8, was located between the lamp and the monochromator to permit high vacuum operation in the monochromator chamber and, thereby, reduce absorption of the radiation by the lamp gas. The chamber contained the entrance slit which was normally set at an opening of 220 μ m. The two differential chambers were pumped by a cold trapped oil diffusion pump.

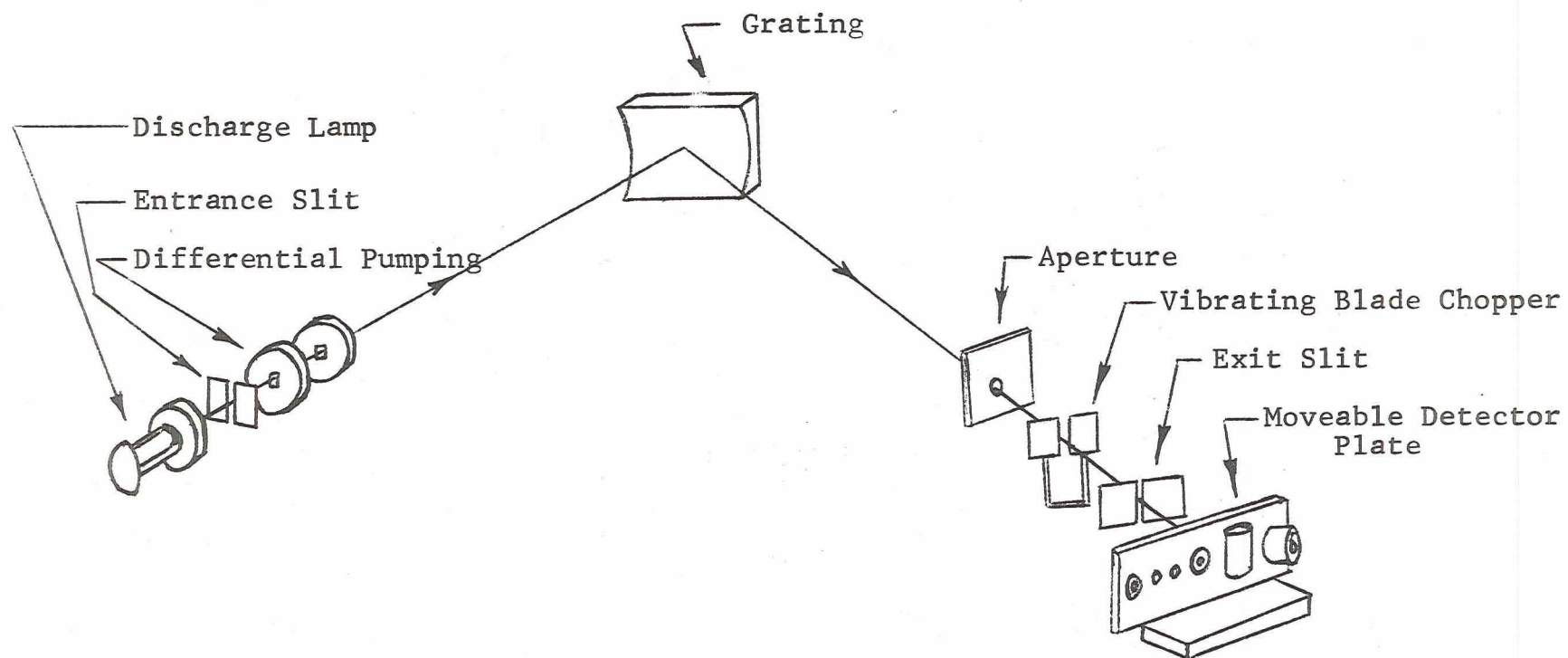


FIGURE 5. SCHEMATIC OF OPTICAL SYSTEM WITH SEYA-NAMIOKA SPECTROMETER.

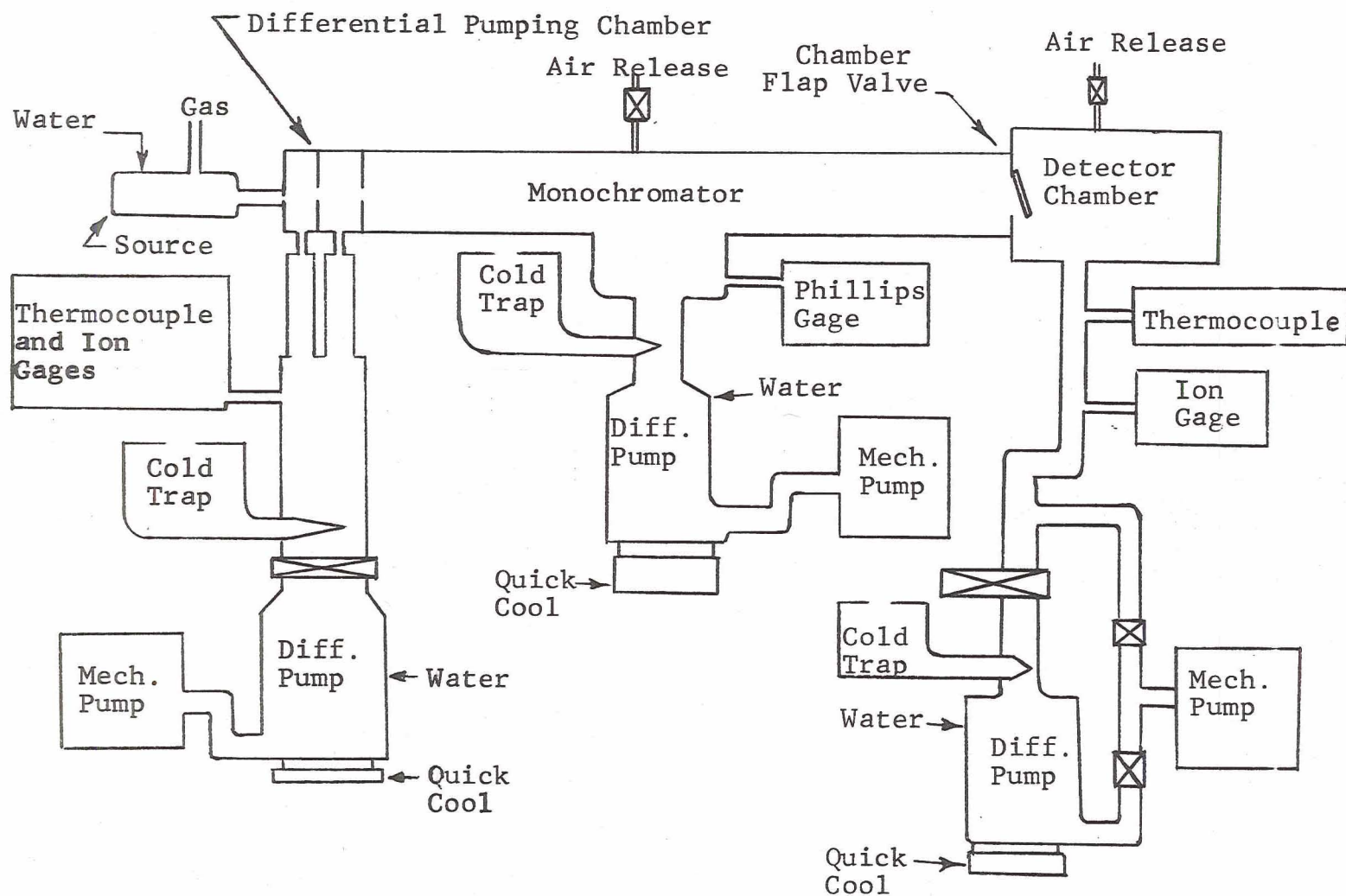


FIGURE 6. DESIGN OF EXPERIMENTAL VACUUM SYSTEM

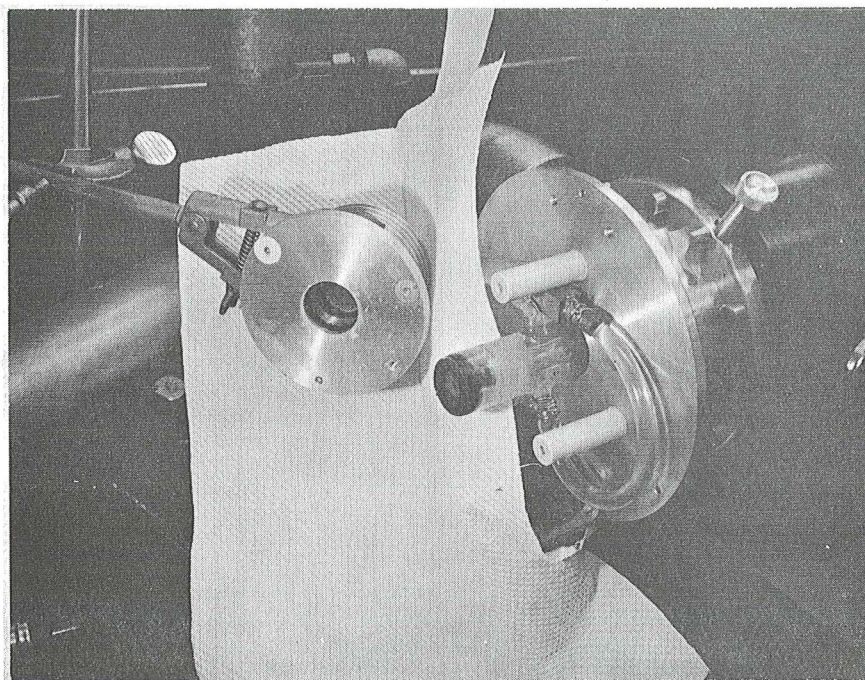


Figure 7. DISASSEMBLED ALUMINUM CATHODE AND QUARTZ CAPILLARY OF THE MCPHERSON UV LAMP.

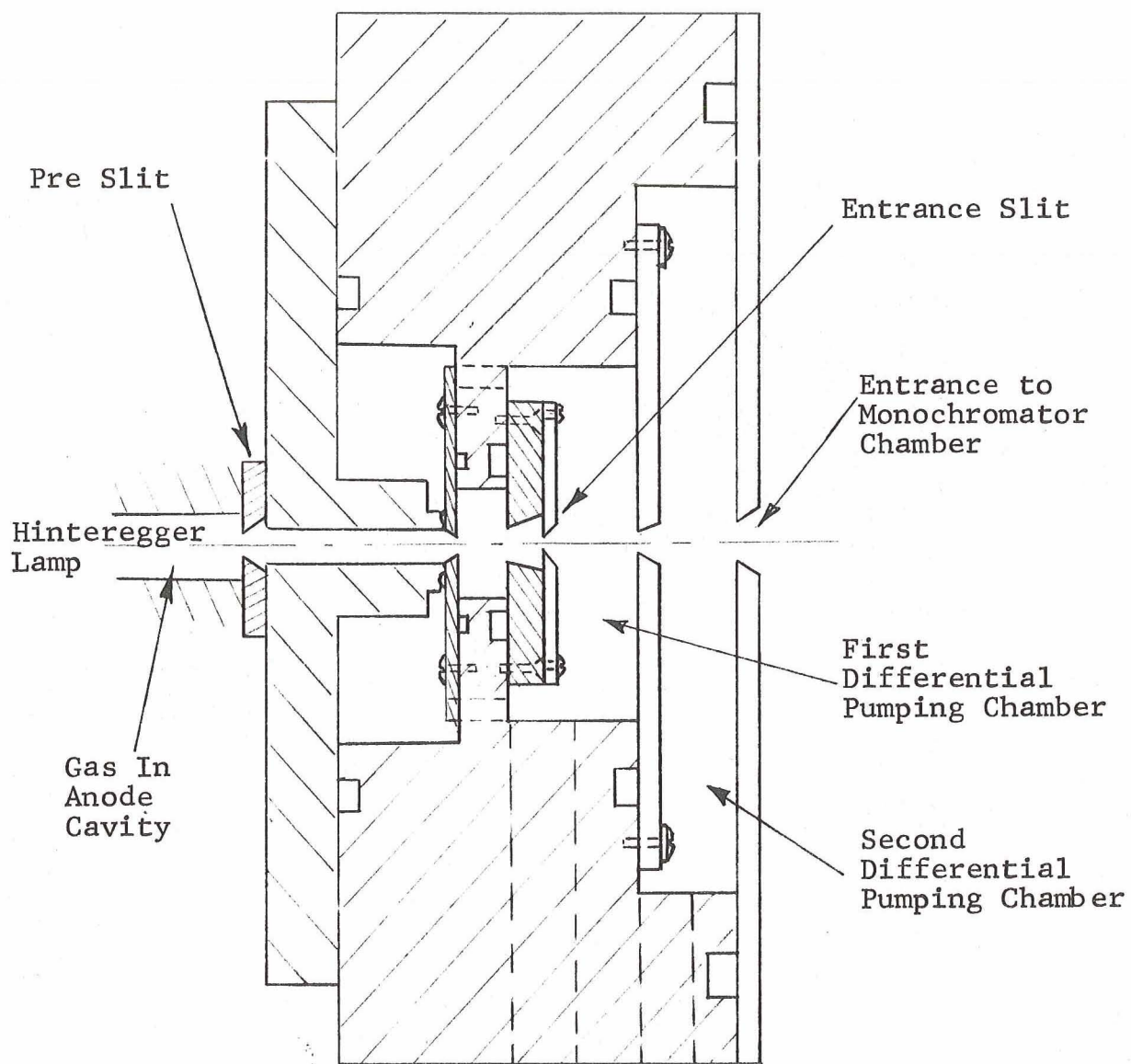


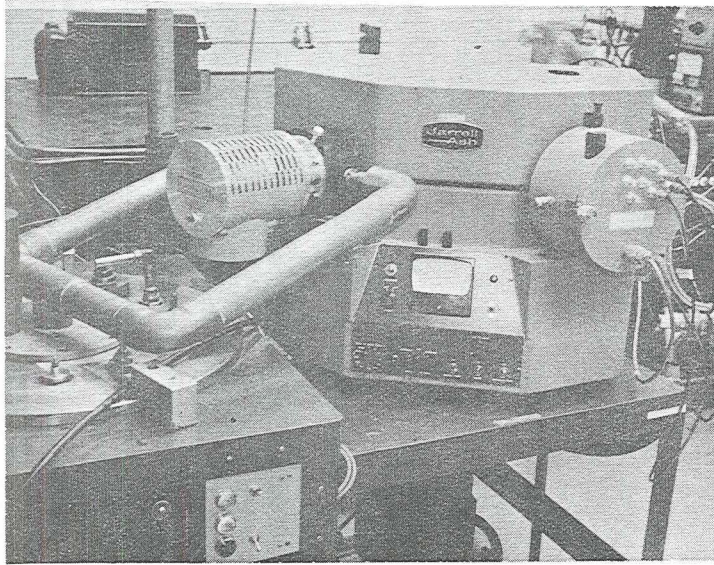
Figure 8. DIFFERENTIAL PUMPING CHAMBER ASSEMBLY

B. Detector Chamber

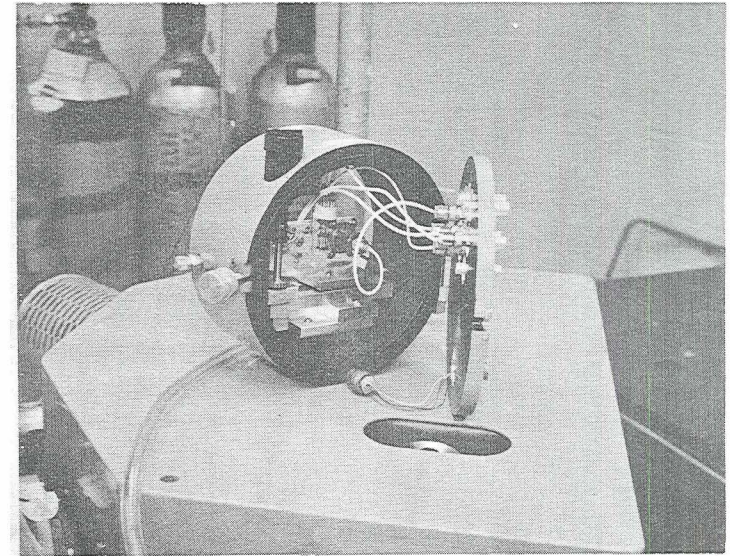
A detector chamber constructed from a modified camera housing was located at the exit plane of the monochromator. Figure 9(a) shows the complete monochromator with the vacuum connections to the differential pumping chamber and the detector chamber. The chamber had a rear door which could be opened for servicing, and the entire chamber, with the exception of the front plate, could be removed and placed on top of the monochromator as shown in Figure 9(b). The detectors were mounted on a dovetail slide which could be driven with a gear linkage and vacuum feedthrough from a knob outside and on top of the chamber, see Figure 9(c). The front plate of the chamber remained continually fixed to the monochromator and to it was mounted an American Time Products Model L40 tuning fork light chopper with a frequency of 150 Hz, Figure 9(d). The chopper had blades that were open to half aperture when not being driven and was aligned to pass the total beam flux to the exit slit when not in operation. In operation it generated a sine wave modulation on the exiting photon beam.

The monochromator exit slit was behind the chopper and mounted in the removable portion of the detector chamber. The detectors which were mounted on the dovetail slide passed behind the slit at a distance of 2 mm from its jaws. Also mounted on the dovetail slide plate were two thermofoil resistance strip heaters and two thermal resistance sensing elements. A rear view of the slide with its components is shown in Figure 10. The slide normally carried the ion chamber, the photomultiplier tube, and interchangeable plates holding various detectors. A 1/4-20 thread screw drove the detector mounting plate along the dovetail ways.

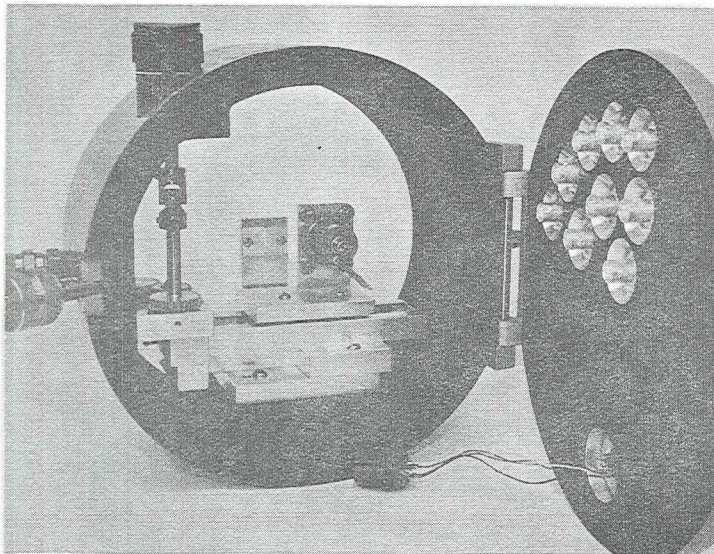
Connections to the detectors were made with miniature coaxial cables and BNC connectors which mated to the BNC feedthroughs installed in the rear door of the chamber. The connections for the ion chamber, the photomultiplier high voltage and anode current, and 5 other detectors can be seen in the photographs of Figure 11. Also mounted in the rear door was an electrical multiple pin instrument feedthrough to provide the 4 leads to power the chopper, 2 leads for powering for heater, and 4 leads for the temperature sensors. During operation it was then possible to continuously monitor the photomultiplier tube output current, the ion chamber current, and connect to any of the other test detectors.



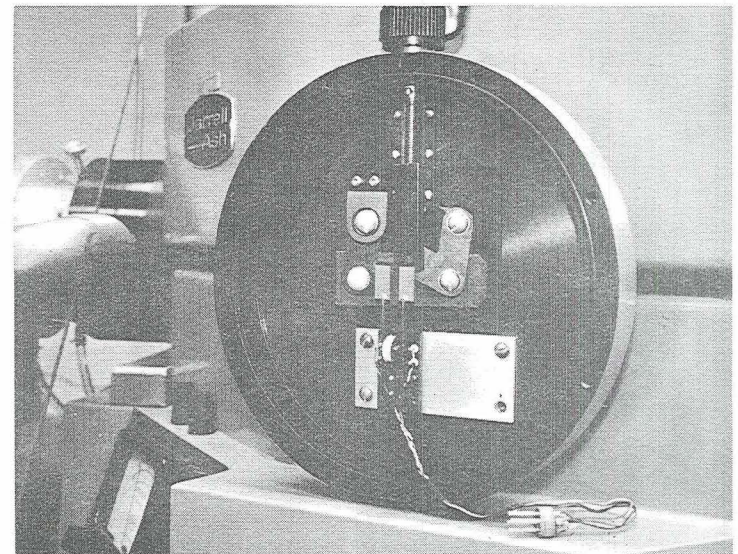
a



b



c



d

Figure 9. EXPERIMENTAL SYSTEM COMPONENTS

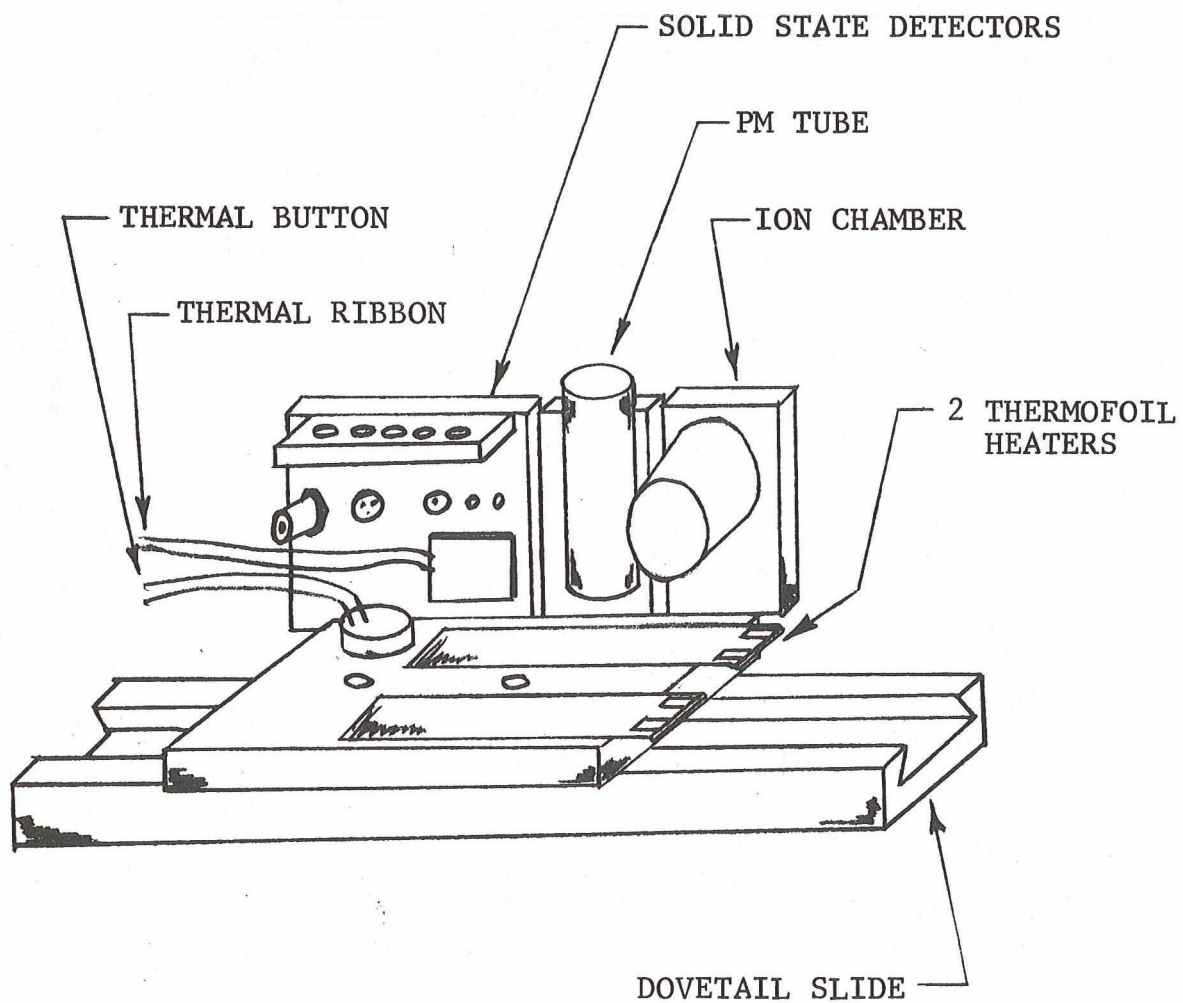
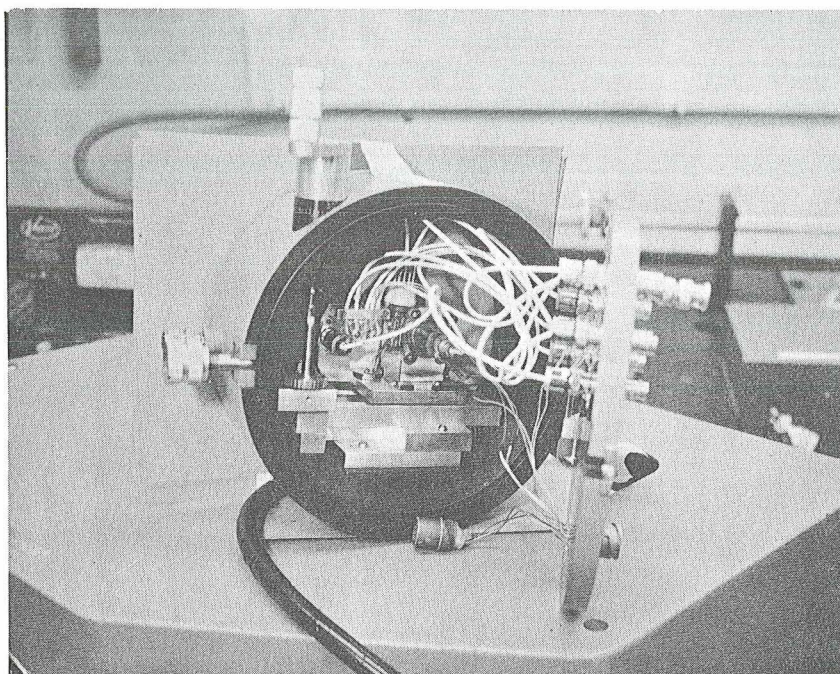
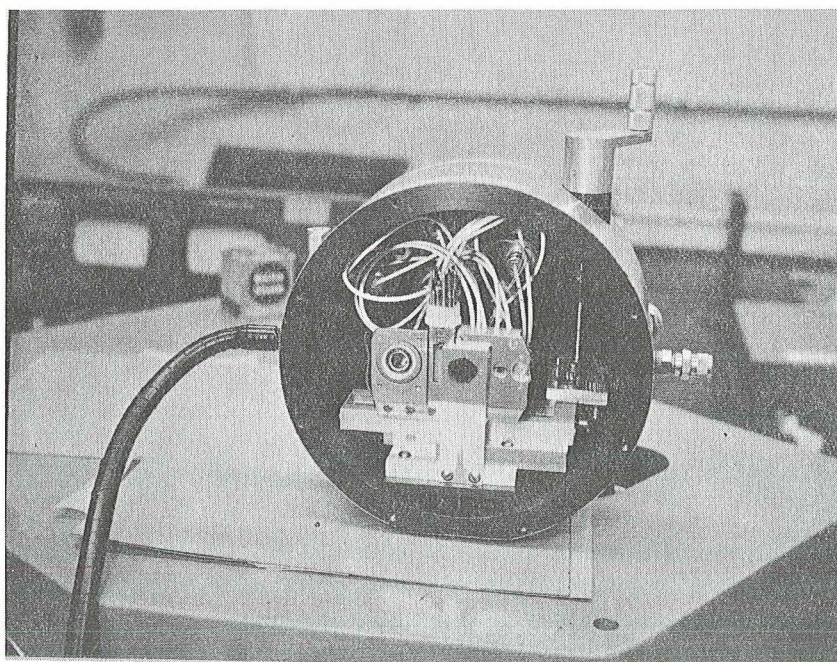


FIGURE 10. REAR VIEW OF HEATER AND TEMPERATURE
SENSOR LOCATIONS.



(A) REAR VIEW OF DETECTOR CHAMBER



(B) VIEW FROM MONOCHROMATOR

FIGURE 11 DETECTOR CHAMBER WITH CONNECTIONS TO REAR DOOR.

C. Detector Electronic System

A schematic of the electronics system components for detector measurements is presented in Figure 12. Before the radiation is incident on any detector it passes between the blades of a chopper which will normally allow the continuous photon beam to pass and, when activated, will modulate it at 150 Hz.

The photodiodes and phototransistors, which are described in the next chapter, were all connected to a battery bias voltage supply of 7 volts. The polarity of the voltage could be switched to provide reverse bias for all the solid state detectors. The detector current passed through a 12 megohm load resistor and a 10 megohm input resistance of a Tektronix Type 122 preamplifier. The preamplifier had a gain of 100 with a signal frequency band pass between 80 and 250 Hz. To reduce any 60 Hz noise pickup the preamplifier was powered by batteries. The stannic oxide crystal had a similar circuit with a 300 volt bias that could be switched in polarity.

The amplified signal from the preamplifier and a signal from the chopper driver were connected to the inputs of a Princeton Applied Research lock-in-voltmeter model JB-5, which synchronously detected the chopped detector signal. The voltmeter output was displayed both on a meter and a chart recorder used to record a spectrum when the monochromator was wavelength scanned.

A sodium salicylate coated photomultiplier tube and a nitric oxide ion chamber were also alternately connected through two Keithley Model 417 picoammeters to the chart recorder. The photomultiplier was operated at minus 1000 volts and the ion chamber at minus 22.5 volts.

A Wheatstone bridge was used to measure the resistance of the two thermal sensors connected to the detector mounting plate. The elements were a Minco thermal ribbon and heater-sensor button. A d.c. power supply was used to supply power levels up to 25 watts to the thermofoil heater elements in the detector chamber.

IV. DETECTORS

Along with the solid state detectors to be tested, a nitric oxide ion chamber and sodium salicylate coated photomultiplier tube were employed to determine the photon beam flux levels through the monochromator exit slit. The nitric oxide chamber measured the absolute photon flux at a wavelength of 1215 angstroms. The photomultiplier could then be used to transfer this flux calibration to other wavelengths.

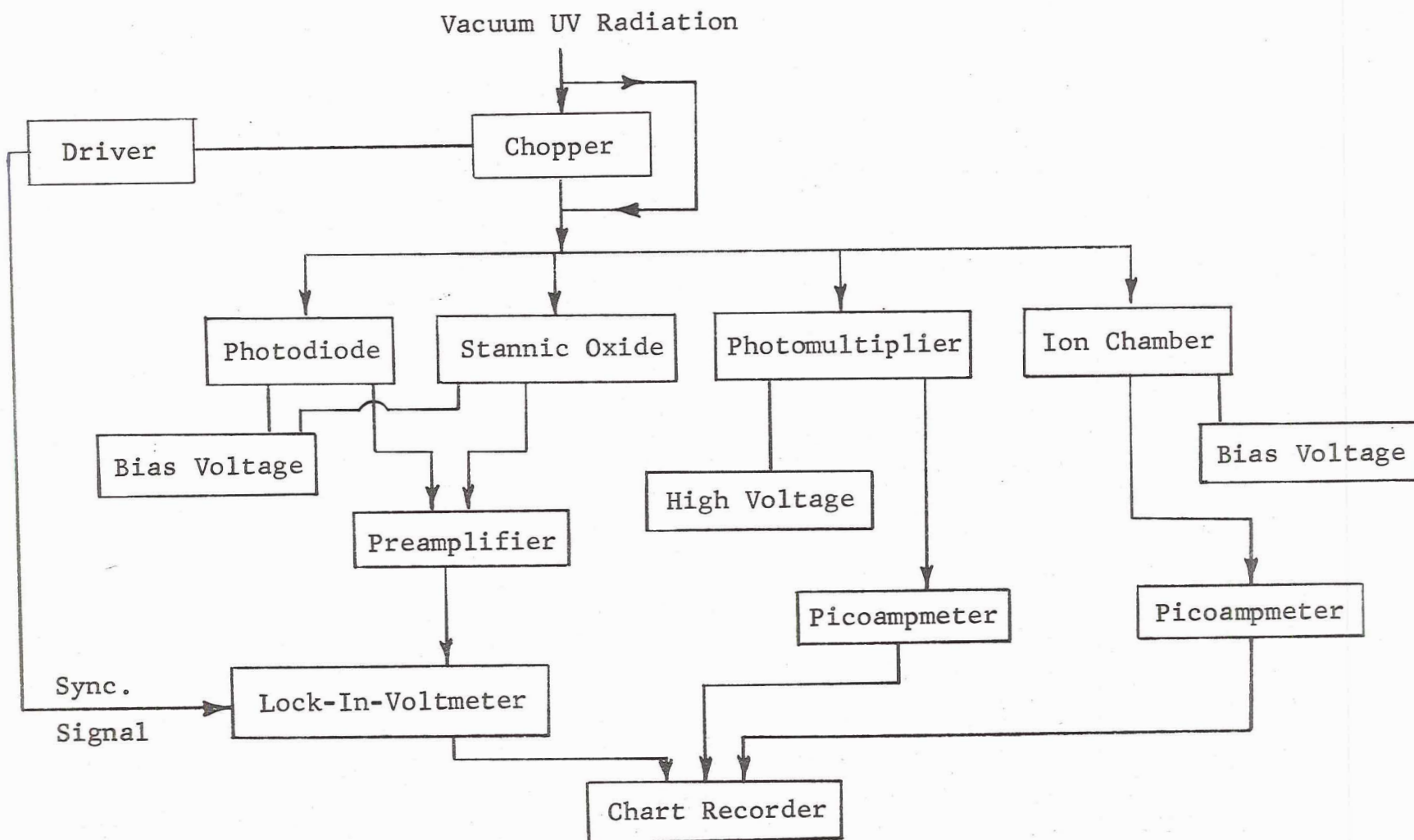


Figure 12 DETECTOR SYSTEM COMPONENTS

Table 2 lists the detectors which were employed during this study.

TABLE 2. DETECTORS

<u>DETECTOR</u>	<u>PROPERTIES</u>
1. Nitric Oxide Ion Chamber	Absolute calibration at 1215 Å.
2. Sodium Salicylate PM Tube	Secondary standard
3. United Detector Technology PIN-Spot/2	Surface barrier detector Two element array, each element 1.0 by 2.3 mm.
4. University of Chicago No. 1490	Surface barrier detector
5. Hewlett Packard Assoc. 5082-4204	Photodiode, diffused junction, 0.508 mm diameter
6. Fairchild FPM 100	Phototransistor, diffused junction, 1.0 sq. mm.
7. Fairchild FPM 200	Photodiode, diffused junction, 1.0 sq. mm.
8. Stannic Oxide Crystal	Crystal photoconductor, 4 mm long

A. Nitric Oxide Ion Chamber

The ion chamber was manufactured by Melpar Inc. and had a rated quantum efficiency for 1215 angstrom radiation of 43.2 percent. The chamber center electrode was biased at a minus 22.5 volts with respect to the grounded outer wall. The photon beam entered the chamber through a 0.75 inch diameter lithium fluoride window. Normal leakage currents at the picoammeter were 4×10^{-13} ampere when no radiation was incident on the chamber.

B. Sodium Salicylate Coated Photomultiplier Tube

A RCA type 8571 photomultiplier tube with its entrance window coated with a layer of sodium salicylate phosphor was employed as a secondary standard. The tube was operated at 1000 V and had a rated sensitivity of 7.3×10^4 A/W for 4000 angstrom radiation. The 8571 is a side-on, 9 stage tube with an S-4 spectral response that matches the emission from the phosphor coating. Normal anode dark currents ranged between 3 and 4×10^{-9} A. Ten 1.0 megohm resistors composed the voltage divider circuit. The absolute quantum efficiency of sodium salicylate for different wavelengths has been investigated by a number of scientists and most recently reported by Bruner.

C. Fairchild FPM 200 Photodiode

The Fairchild FPM 200 photodiode is a silicon planar passivated detector which is mounted in a two terminal coaxial package that is 2 mm in diameter and 4.4 mm long. The front window of the case was removed so the ultraviolet radiation would be incident directly on the 1.0 mm square silicon chip. An electrode is connected to the front surface of the chip as can be seen in Figure 13,A. All diodes were operated in the reverse bias mode as shown in Figure 14,A. The FPM 200 was connected with the circuit of Figure 14,B to a 7 volt bias battery. The response risetime is rated at 3μ sec. Maximum rated operating temperature range is between -65° C and $+200^{\circ}$ C. By contact packing these devices they can be assembled into a linear array of discrete element detectors.

D. Fairchild FPM 100 Phototransistor

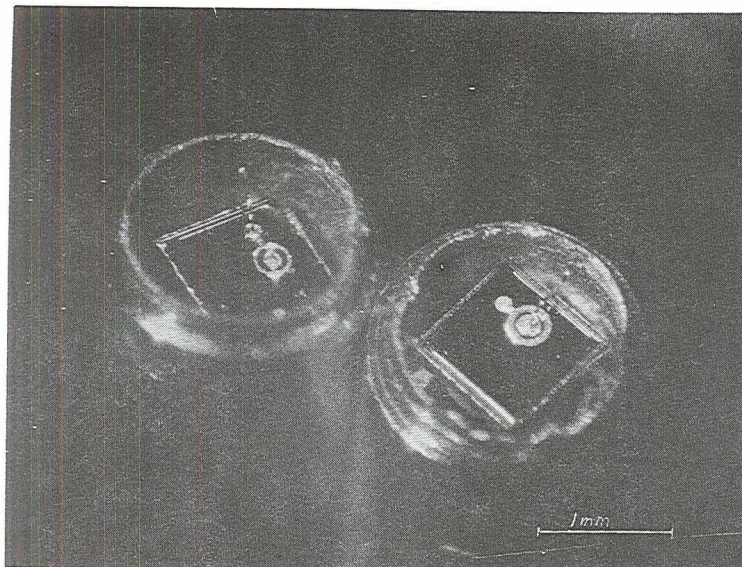
The Fairchild FPM 100 phototransistor is a silicon NPN planar passivated detector mounted in the same size two terminal coaxial case as the FPM 200. The window was again removed and the 1.0 mm square silicon chip can be seen in Figure 13,A. The emitter and collector were connected as shown in Figure 14,E. Normal operating collector-emitter bias was 7 volts. The same temperature ratings as the FPM 200 photodiode apply and they can be assembled into similar arrays. Response risetime is rated at approximately 3μ sec.

E. United Detector Technology PIN-Spot/2 Photodiode

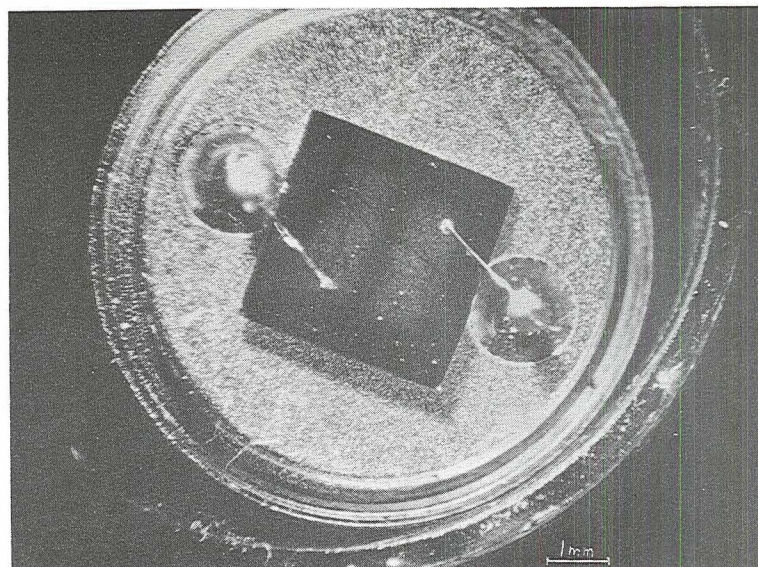
The PIN-Spot/2 was a special ultraviolet sensitive silicon Schottky barrier photodiode with two 1.0 by 2.3 mm elements separated by 0.3 mm on a single chip. Figure 13,B is a photograph of the detector surface. The surface electrode is a layer of gold on the order of one hundred angstroms thick. Electrical connection to the elements is shown in Figure 14,C. A 7 volt reverse bias was employed. The response time is rated in the nanosecond region and the junction capacitance is less than 5 picofarads per element. The detector is mounted in a TO-5 can with 3 leads. The elements are representative of larger arrays which can be fabricated on single silicon chips. The detector elements are very similar in construction to the University of Chicago photodiode described in a later section.

F. Hewlett Packard 5082-4204 PIN Photodiode

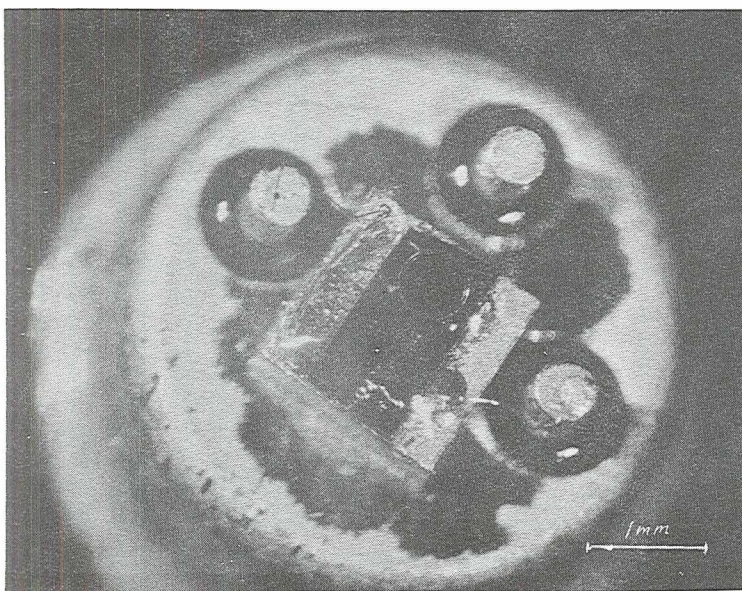
The PIN photodiode is a silicon planar device with a 0.5 mm diameter p-region shown in Figure 13,C. The window of the container and a layer of Sylgard 182 which covered the silicon chip were removed. The device connections and its electrical schematic are presented in Figure 14,D. Typical response at 7700 Å for a 25° C operating temperature is 0.75



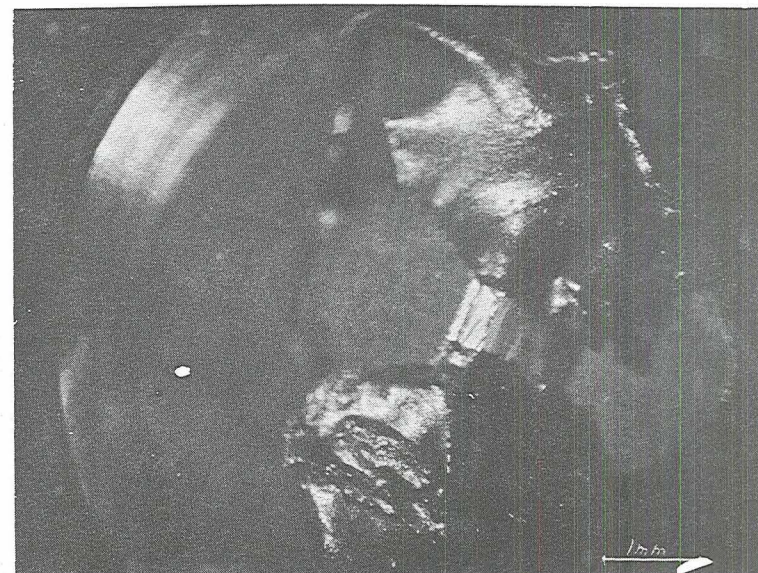
(A) FPM 200 (LEFT) AND FPM 100 (RIGHT)



(B) UDT PIN SPOT-2, 2 ELEMENTS

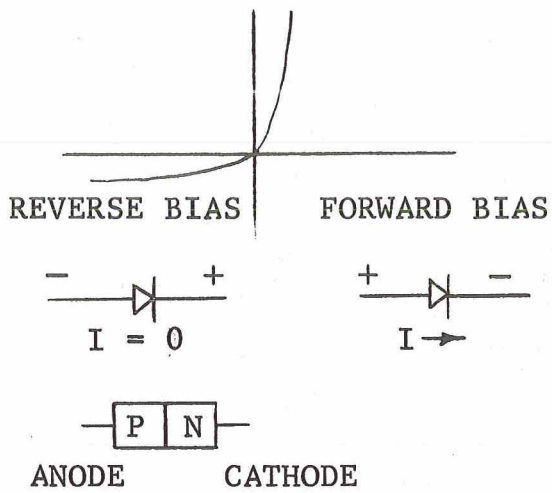


(C) HPA 5082 - 4204

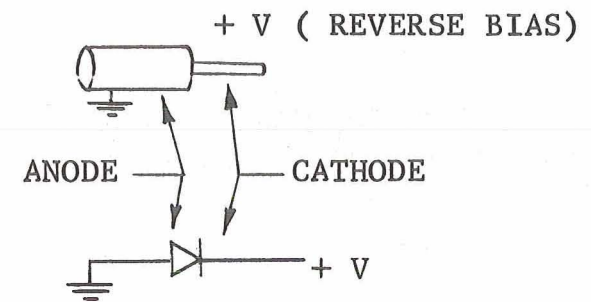


(D) STANNIC OXIDE CRYSTAL

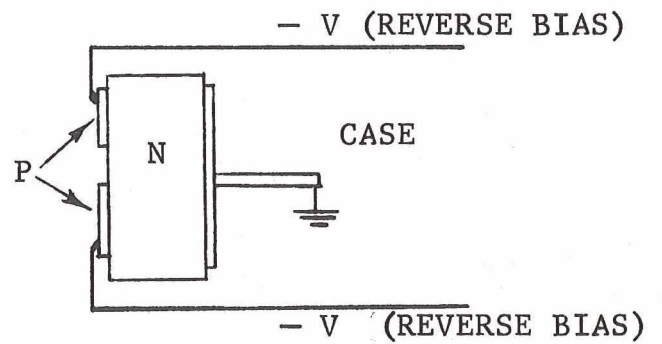
FIGURE 13 DETECTOR ELEMENTS



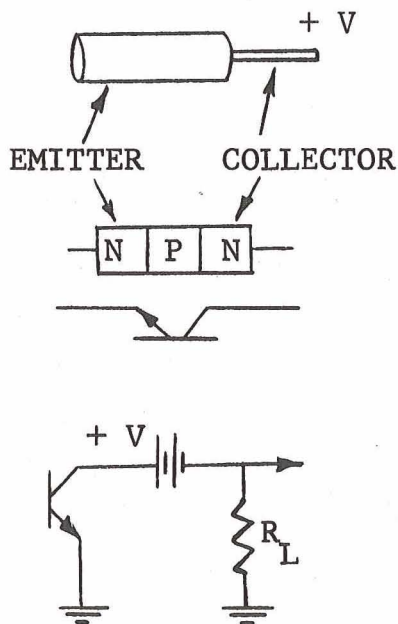
(A) DIODE OPERATION



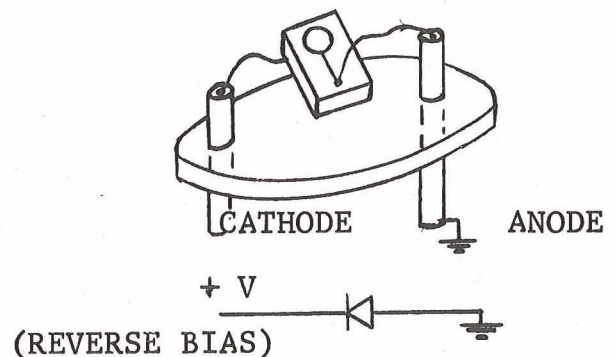
(B) FPM 200 FAIRCHILD
PHOTODIODE



(C) UDT PIN SPOT-2 PHOTODIODE



(E) FPM 100 FAIRCHILD
PHOTOTRANSISTOR



(D) HPA 4204 PHOTODIODE

FIGURE 14 SOLID STATE DETECTOR CONNECTIONS.

electrons per photon or 0.5 A/W ($1.0 \mu \text{ A/mW/cm}^2$). The sensitive area is $2 \times 10^{-3} \text{ cm}^2$ and the rated noise equivalent power, NEP, is $1.2 \times 10^{-14} \text{ W}$. Leakage or dark currents were rated at 400 pA maximum with a 2 pF junction capacitance.

Measurements have been made by E. Whiting, et. al. with the 4204 over the spectral range of 4400 to 2000 Å and indicated a drop in relative response at 2000 Å of only 50 percent from that at 4000 Å.⁷ The quantum efficiency at 2000 Å was reported to be 0.37 electrons/photon. Stability of these devices over a period of weeks was also found to be quite good. The measuring system employed a 200 Hz chopper with synchronous detection and a deuterium lamp.

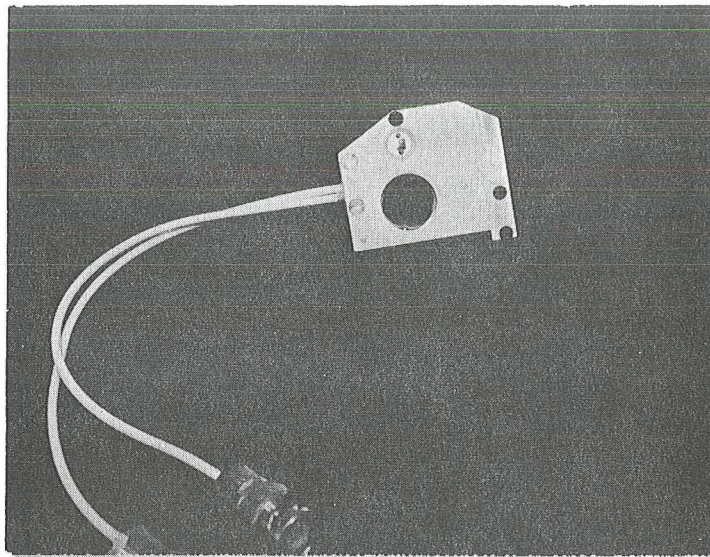
G. Stannic Oxide Crystals

The stannic oxide crystals were provided by RCA Laboratories and investigated because of their sensitivity at 2850 Å and an energy gap of 4.3 eV which causes them to be solar blind. Detectivities measured at 2850 Å by the RCA group were as high as $8 \times 10^{12} \text{ cm watt}^{-1} \text{ Hz}^{1/2}$ for a 25 Hz modulated photon beam and a 1 Hz bandwidth.^{8,9} NEP's for that wavelength were on the order of 10^{-12} watt .

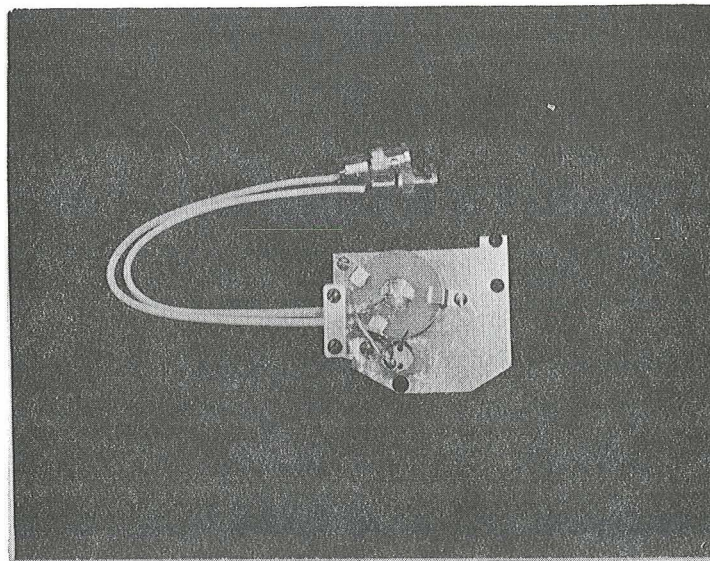
The crystal used for the current study had an exposed area of about 0.25 mm^2 . It was mounted on a modified coaxial feedthrough and had its ends electrically connected with conductive epoxy, see Figure 13,D. A bias voltage of 300 V was applied across the crystal.

H. University of Chicago Silicon Photodiode

This detector was a silicon surface barrier photodiode No. 1490 with a 19 mm diameter sensitive area that was fabricated in about 1964 by A. J. Tuzzolino at the University of Chicago. The photodiode is n-type silicon with approximately a 100 Å thick gold film front electrode. Two publications describe operation in the 584 to 2500 Å region, with similar devices made during the same period.^{10,11} The detector employed for these measurements had a dark current of 5×10^{-7} at 6 volts reverse bias and rated sensitivities of 0.40 electron/photon at 4358 Å and 0.47 electron/photon at 5461 Å. Figure 15 shows the diode mounted next to a UDT detector on a plate for insertion into the monochromator system.



a. Front view of mounted photodiode and UDT detector.



b. Rear view of detectors.

Figure 15. UNIVERSITY OF CHICAGO PHOTODIODE

V. MEASUREMENT ANALYSIS METHOD

To determine detector performance the incident photon flux, $N_o(\lambda)$, is obtained by using the nitric oxide ion chamber at the 1215 Å line. The flux is calculated by measuring the change in ion chamber current, I_1 , between the background and the photon beam current. The number of photons per second is then found by

$$N_o(\lambda) = \frac{I_1}{\eta_1 q}, \text{ photons/sec.}$$

where η_1 is the quantum efficiency of the ion chamber, 43.2%, and q is the electronic charge, 1.6×10^{-12} coulomb. Typical photon fluxes were 3×10^7 photons/sec. through a 0.55 by 0.8mm rectangular aperture at the exit plane of the monochromator. Beam power $P(\lambda)$ is then calculated by

$$P(\lambda) = N_o(\lambda) E(\lambda), \text{ watts}$$

where $E(\lambda)$ is the photon energy at that wavelength. For a wavelength of 1215 Å, $E(\lambda)$ is 1.64×10^{-18} joule and the above typical photon flux corresponds to a power of 4.92×10^{-11} watt.

The RCA 8571 photomultiplier tube with a sodium salicylate window can then be positioned in the calibrated photon beam and its anode current measured. This current measurement is then subtracted from the PM tube background to obtain the photon generated current I_2 at 1215 Å. The total sodium salicylate photomultiplier tube detector quantum efficiency η_2 is then found by

$$\eta_2 = \frac{I_2}{N_o(\lambda) q}, \text{ electrons/photon.}$$

Since the response of the sodium salicylate is known in the 300 to 2000 Å region this detector can be employed as a secondary standard to measure the photon fluxes at wavelengths other than the 1215 Å, which is the only wavelength calibrated for the ion chamber.

Upon absorption of the vacuum ultraviolet photon the excited sodium salicylate phosphor emission spectrum is centered at 4000 Å which is the wavelength of peak response for the S-4 photocathode of the photomultiplier tube. The absolute luminescence quantum efficiency; i.e., the ratio of the number of luminescence emission photons emitted to the number of excitation photons is approximately 40 percent. However, the percent

of emission photons which arrive at the PM photocathode is considerably reduced due to spherical radiation from the phosphor and the limited acceptance angle of the photocathode. Reabsorption and scattering inside the phosphor layer also contributes to the reduction in total system quantum efficiency. When employing the total PM tube detector it is only necessary to know the relative phosphor quantum efficiency with respect to wavelength.

Sensitivity, S , of a detector is defined as the photocurrent per input power and is given by

$$S = \frac{I}{P(\lambda)}, \text{ amp/watt.}$$

The sensitivity of the solid state detectors is found by measuring the modulated output photocurrent from the detector and dividing by the input photon power.

The relative quantum efficiency η_3 , of the solid state detectors is found by

$$\eta_3 = \frac{I}{N_o(\lambda) q}, \text{ electron/incident photon,}$$

where I is the average photocurrent from the detector. Since the number of incident photons which are reflected from the detector face is unknown the absolute quantum efficiency cannot be determined; however, this measurement is not required for design of the spectrometer detectors.

The photocurrent from the detector is determined by measuring the output signal from the Princeton Applied Research lock-in-voltmeter. The measuring system was calibrated by applying a known signal voltage to the input of the detector bias box and recording the lock-in-voltmeter outputs. The signal current through the load resistors could then be calculated.

VI. MEASUREMENT RESULTS

The detectors were mounted in various groups on aluminum plates that were located next to the sodium salicylate coated photomultiplier tube and the ion chamber in the detector chamber at the monochromator exit plane. They then could be alternately scanned or positioned behind the monochromator exit aperture. Normal operation was with the 150 Hz chopper and a 1.0 Hz bandwidth.

A. Sensitivity and Minimum Detectable Power

To calibrate the monochromator wavelength drive, the spectrum was scanned with the sodium salicylate photomultiplier tube fixed behind the exit slit. The resulting helium emission spectrum is presented in Figure 16 and shows the HeI line at 584.3 Å and its doubling at 1168.6 Å. Also clearly present are lines at 1025 and 1215.7 Å from hydrogen which was an impurity present in the lamp.

For comparison the solid state surface barrier photodiodes were also scanned through the same spectral region. Figure 17 is the helium emission spectrum obtained from the University of Chicago (U of C) photodiode No. 1490. The spectrum has substantially the same shape as that from the sodium salicylate coated photomultiplier tube with the exception of a higher response to the 584.3 Å HeI line. Since the sodium salicylate has a relatively constant luminescence quantum efficiency across the spectral region, the surface barrier detector must have an increasing sensitivity from 1215 to 500 Å. Also, since the line at 1751 Å is visible this surface barrier detector does appear to be usable over the entire 500 to 2000 Å region.

A similar spectral scan was made with the United Detector Technology PIN-Spot/2, No. 2 (UDT-2) detector and the same increase in response at 584.3 Å was found. The spectrum which is shown in Figure 18, has a higher noise level than the previous, and consequently, many of the low intensity lines cannot be seen.

Measurements were then made with the detectors by using the 584.3 and 1215.7 Å emission spectral lines which were obtained from He and H in the lamp. Spectral scans were made to obtain the wavelength dependence. The detector data was then analyzed as described in the previous chapter and the spectral quantum efficiency curves of Figure 19 plotted. The dashed curve represents the previous University of Chicago measurements^{10,11} which correlated with current measurements using the U of C No. 1490 detector. The United Detector Technology PIN-Spot/2 No. 1, element A (UDT 1-A) curve has the general form of the U of C, but the UDT-2 detector appeared to have considerably higher sensitivity than its mate.

The stannic oxide crystal also showed a fairly high sensitivity; however, as will later be described, the response was quite unstable. For this reason only a limited number of tests were performed with this detector.

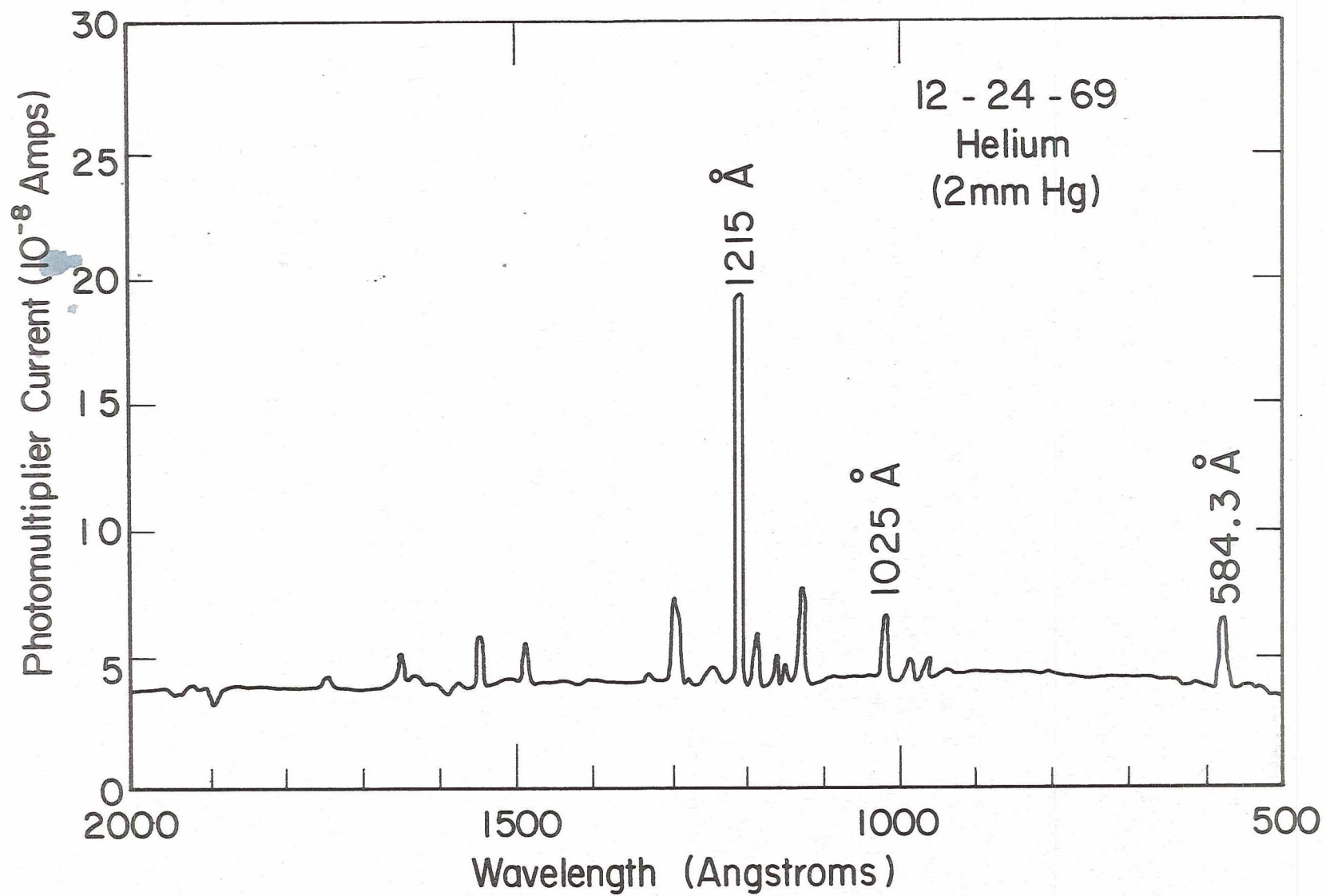


Figure 16. HELIUM EMISSION SPECTRUM BETWEEN 500 AND 2000 ANGSTROMS

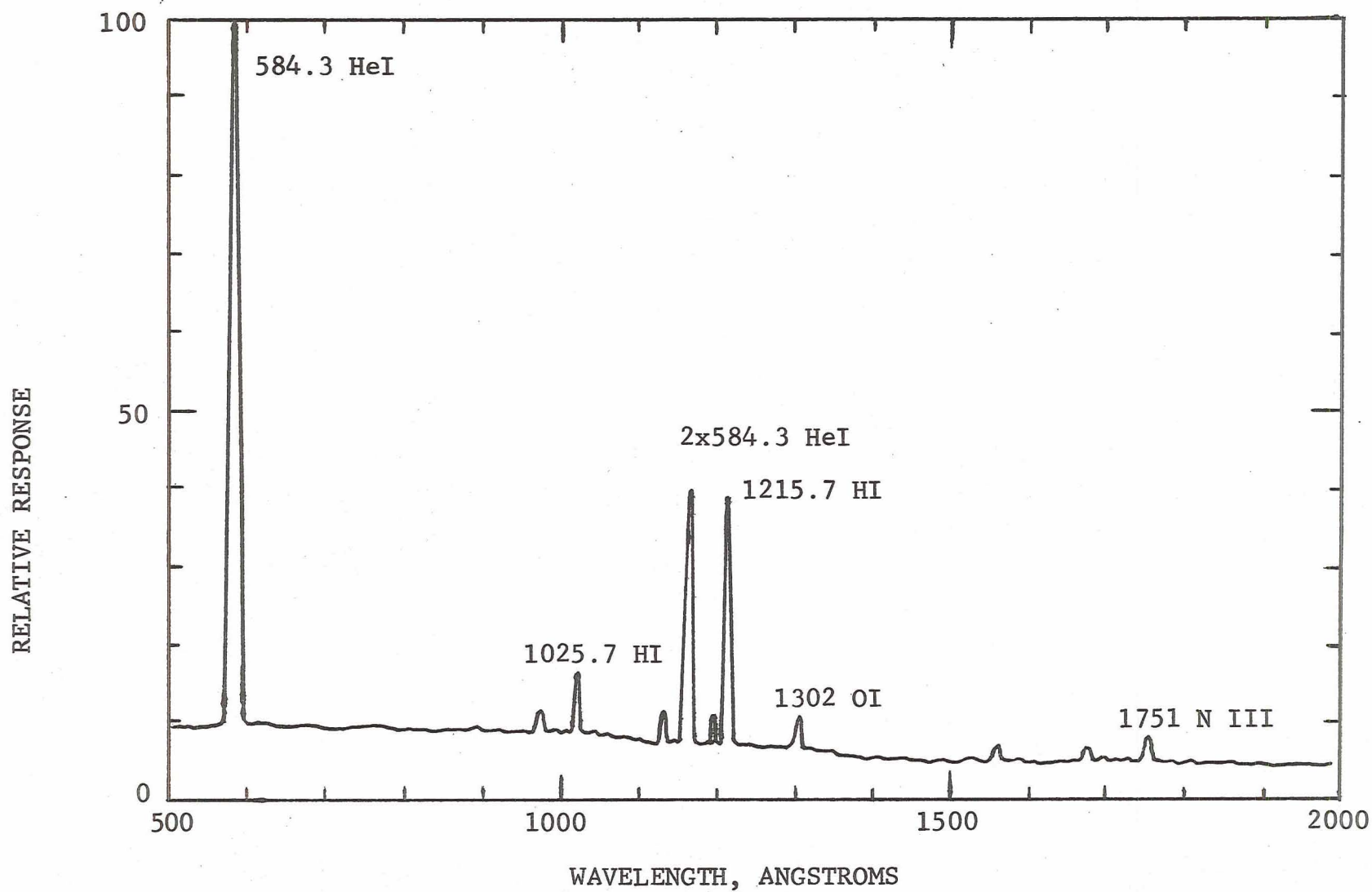


FIGURE 17. HELIUM SPECTRUM FROM THE U OF C PHOTODIODE NO. 1490
AT 7V REVERSE BIAS. EXIT SLIT IS 0.55 BY 10mm. (RUN 10).

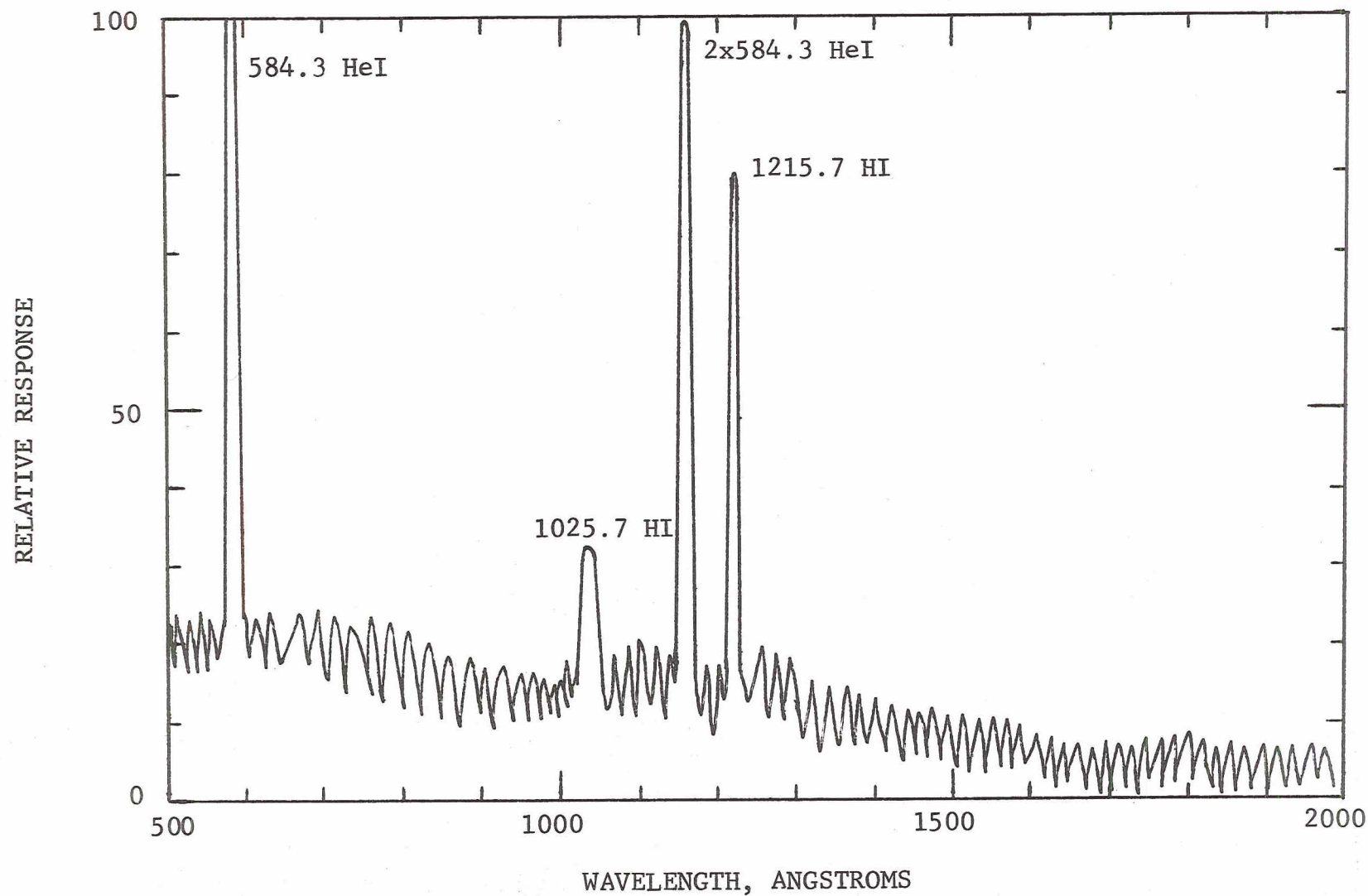


FIGURE 18. HELIUM SPECTRUM FROM THE UDT-2 PHOTODIODE AT 7V REVERSE BIAS. EXIT SLIT IS 0.55 BY 10mm. (RUN 11).

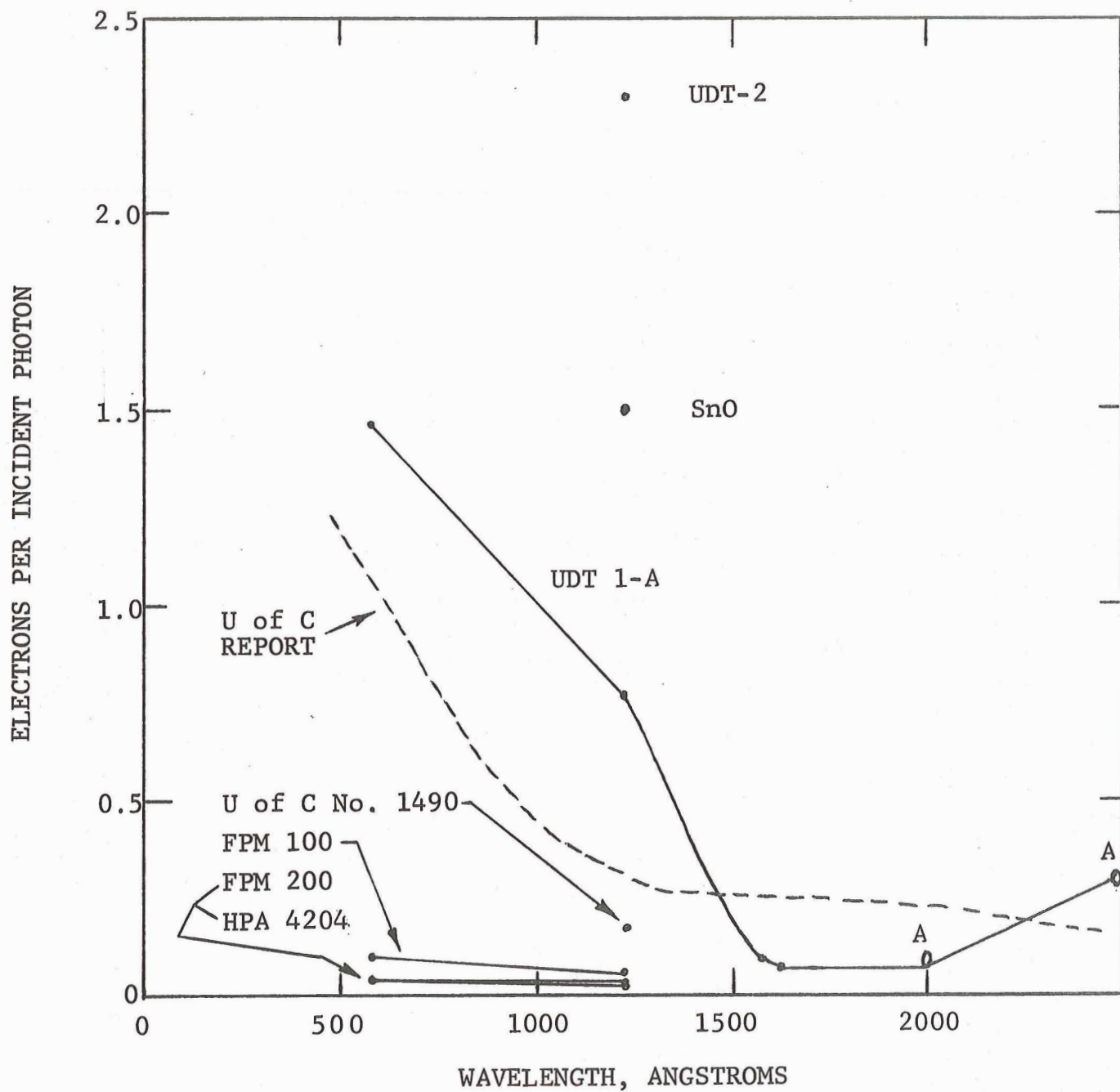


Figure 19. SPECTRAL QUANTUM EFFICIENCY FOR VARIOUS DETECTORS. POINTS A ARE THE MANUFACTURERS SPECIFICATIONS FOR THE UDT.

Values of the HPA 4204 and the FPM 100 and 200 quantum efficiencies in Figure 19 reflect the detectors' diffused junction construction which results in thicker surface layers. Consequently, their quantum efficiencies lie in the 0.1 electron/incident photon range between 500 and 1400 Å, while for the rest of the spectrum region the detector signals were below the noise.

For a more informative presentation of the detectors performance the spectral sensitivity is plotted over the 500 to 10,000 Å region in Figure 20. The vacuum UV data was supplied by this study and the triangular points were obtained from the manufacturers specifications and other investigators' measurements. Because of the relative transparency of silicon above 4000 Å all the detectors have similar performance; however, in the region of minimum sensitivity which was at 1600 Å for the UDT-1, the detector performance should be highly dependent on the device structure. It should then be expected that the three lower curves for the FPM 100, HPA 4204, and FPM 200 would also experience a minimum between 1215 Å and 2000 angstroms.

The minimum detectable power can be best described by the noise equivalent power (NEP) which is the rms (root-mean-square) value of the modulated radiant power incident on the detector that generates an rms current equal to the rms noise voltage from the detector. Thus, the NEP is equal to the beam power required to produce a signal-to-noise ratio (S/N) of one. The S/N ratio is the average signal level divided by its standard deviation. Human observers can usually detect the presence of a signal when the S/N is above five.¹² For a detector the NEP can be expressed as

$$NEP = \frac{i_n}{S}$$

where i_n = rms detector noise current.

S = sensitivity in amp/watt.

The important factor when determining the NEP of detectors is to know if the limiting noise is generated by the detector itself or by the other components of the measuring system. When the detector noise is the limiting factor the NEP can be determined by the S/N of the detector output. The following chapter on noise consideration gives a further explanation and shows that the detector 1/f noise is the limiting factor in the frequency range of interest.

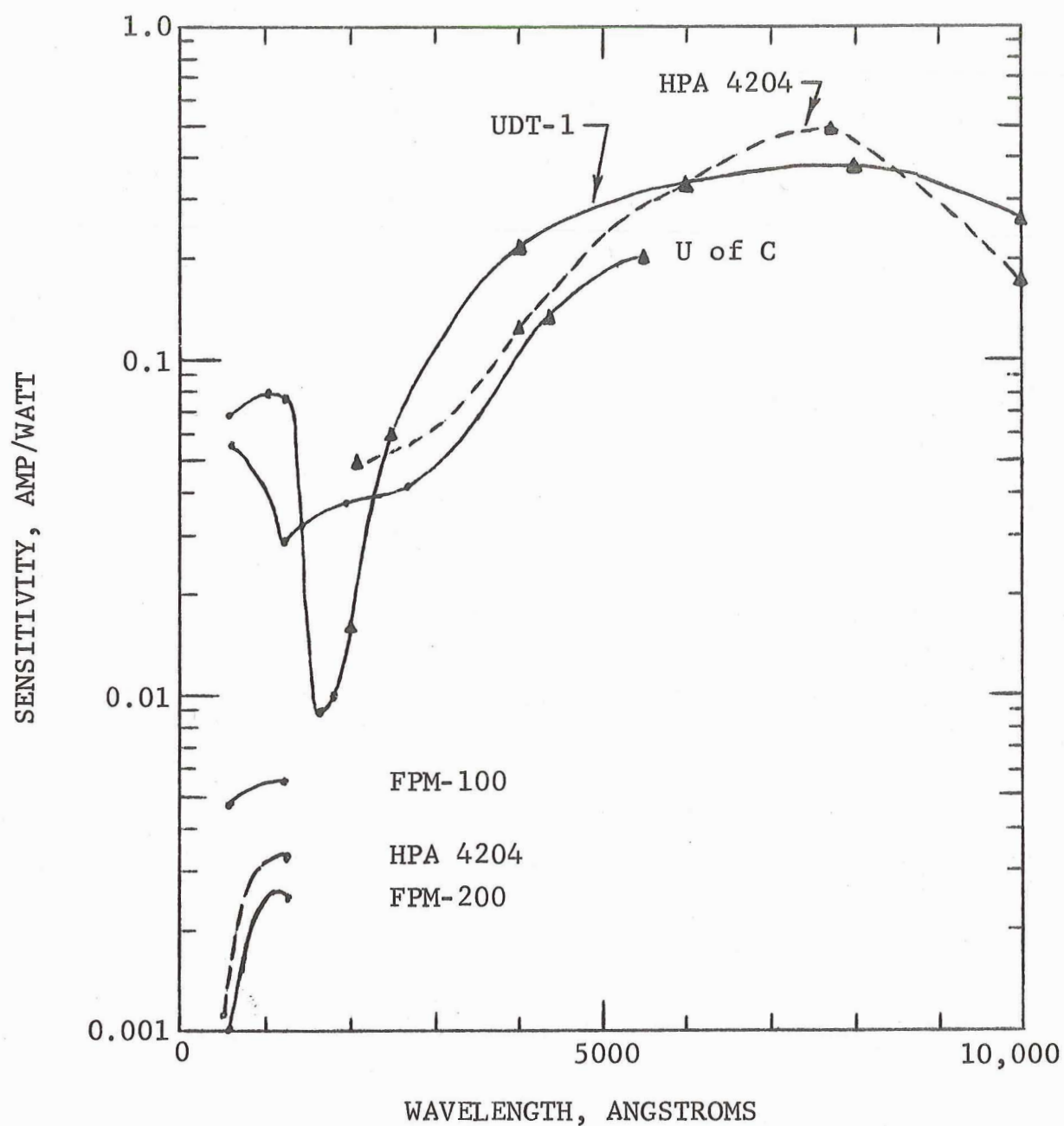


FIGURE 20. SPECTRAL SENSITIVITY OF SOLID STATE DETECTORS. DOTS ARE EXPERIMENTAL MEASUREMENTS AND TRIANGLES ARE MANUFACTURERS SPECIFICATIONS. FREQUENCY 150 Hz, BANDWIDTH 1 Hz FOR EXPERIMENTAL DATA.

Based on the experimental measurements, the NEP at 1215 Å for the various detectors is given in Table 3.

TABLE 3. NOISE EQUIVALENT POWER

Wavelength is 1215 Å.

<u>DETECTOR</u>	<u>NEP (10^{-11} watt)</u>
UDT-1	1.6
UDT-2	0.2
FPM 100	0.9
FPM 200	2.0
HPA 4204	1.5
SnO *	11.0

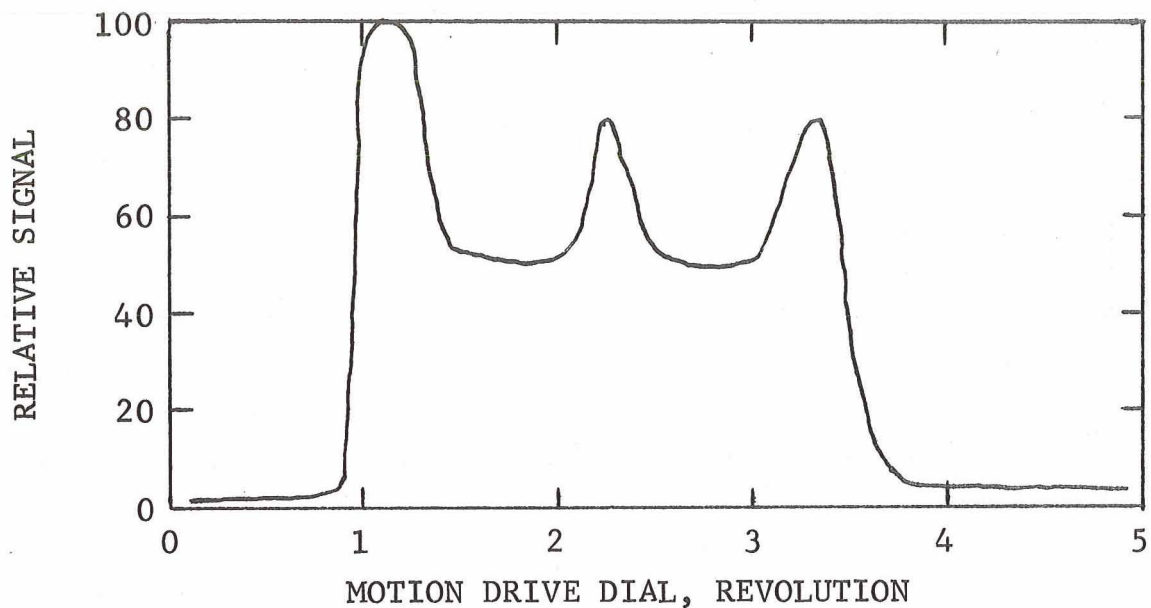
* Bias on stannic oxide was -300 V.

The NEP's for other wavelengths can be obtained from the previous equation.

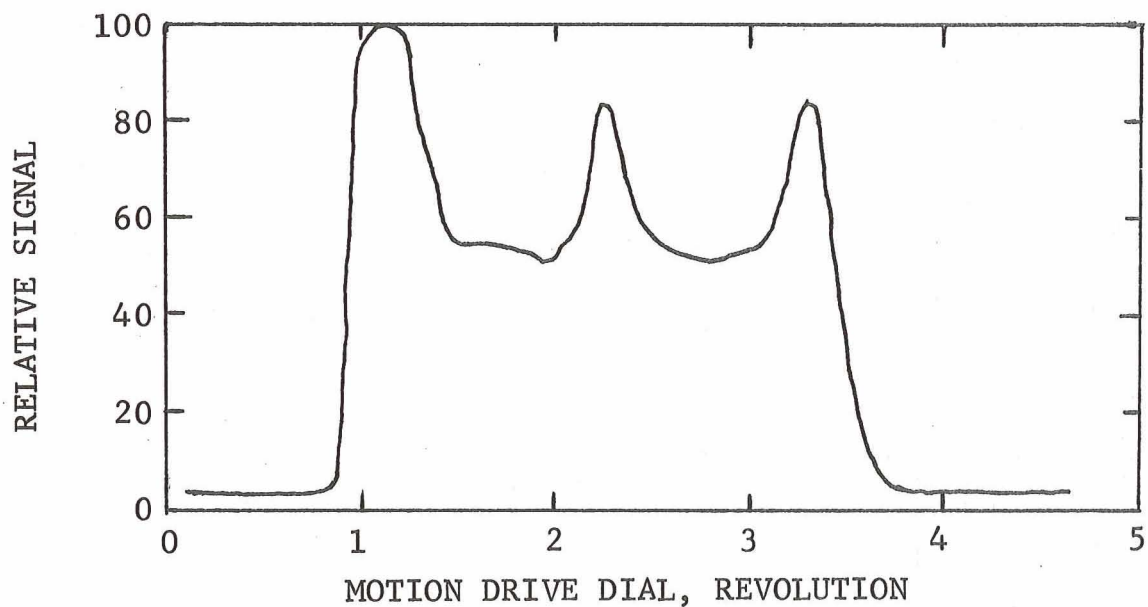
B. Array Elements

The UDT PIN-Spot/2 detectors containing the two elements, referred to as A and B, mounted on the same chip were moved past the monochromator exit slit with the dovetail slide drive to determine the variation in sensitivity and the amount of crosstalk between the elements. One element was connected to the detector electronics system and its output displayed on the chart recorder, while the other element was grounded or left electrically open. Figures 21 and 22 are position scans across the array of the UDT-1 detector for 584.3 and 1215.7 Å respectively, when one detector element was ungrounded. The exit slit was 0.25 mm wide and aligned to the long axis of the detector elements. The motion scans show that there is very little difference which element is used since the cross-talk is approximately 100%. The response variation between elements was 20% for this detector. The distance over which the output signal existed corresponded to a detector motion of approximately 3.25 mm. This was in accord with the total exit beam and detector element width.

A more application-oriented measurement of the cross-talk is presented in Figure 23, where the unused element is grounded. This would probably be the type of operation in a spectrometer since the elements would each have load resistors connected to ground. The dashed curve shows the difference

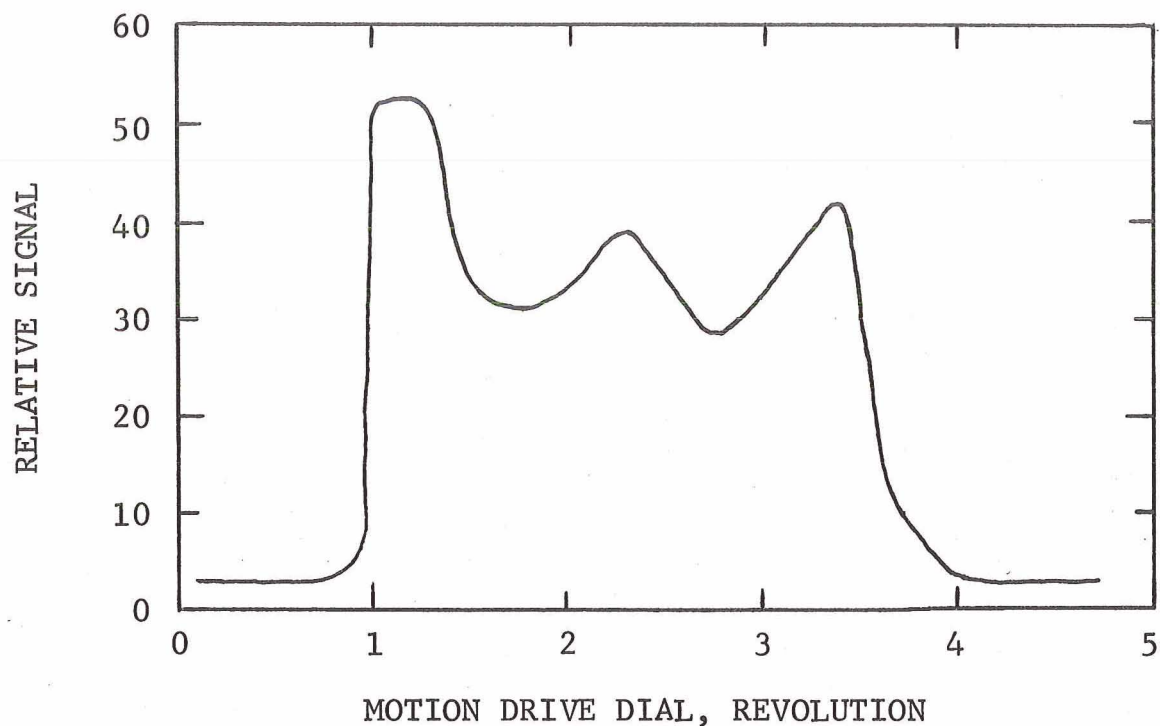


(a) Scan of Element UDT 1-B, Element UDT 1-A is Open.

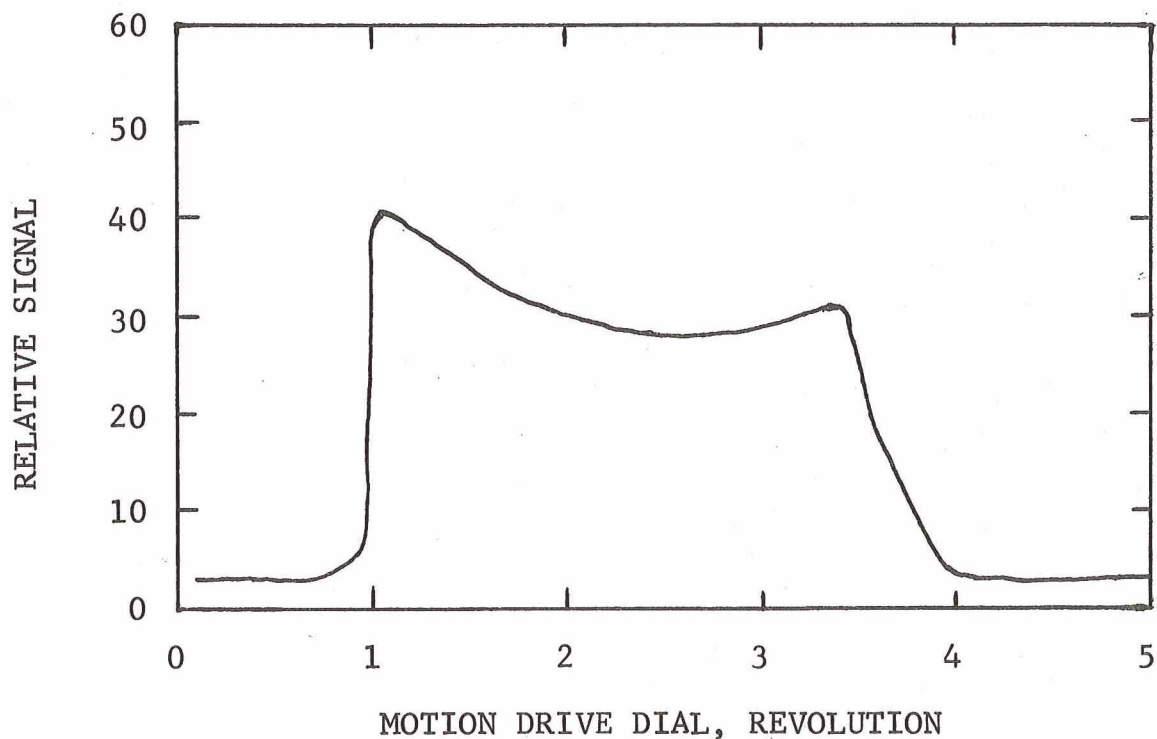


(b) Scan of Element UDT 1-A, Element UDT 1-B is Open.

FIGURE 21. DETECTOR SCANS BEHIND 0.25mm WIDE EXIT SLIT WITH 584.3 Å RADIATION. OTHER ELEMENTS ARE OPEN AND ONE DIAL REVOLUTION EQUALS A DETECTOR MOTION OF 1.26mm. (RUN 39).

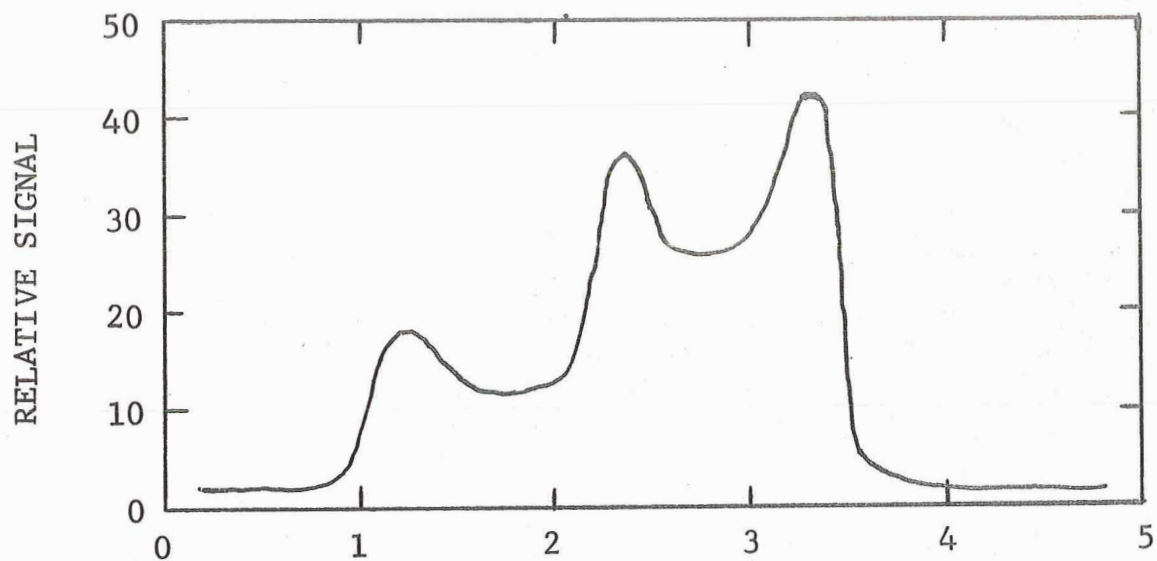


(a) Scan of Element UDT 1-A, Element UDT 1-B Open

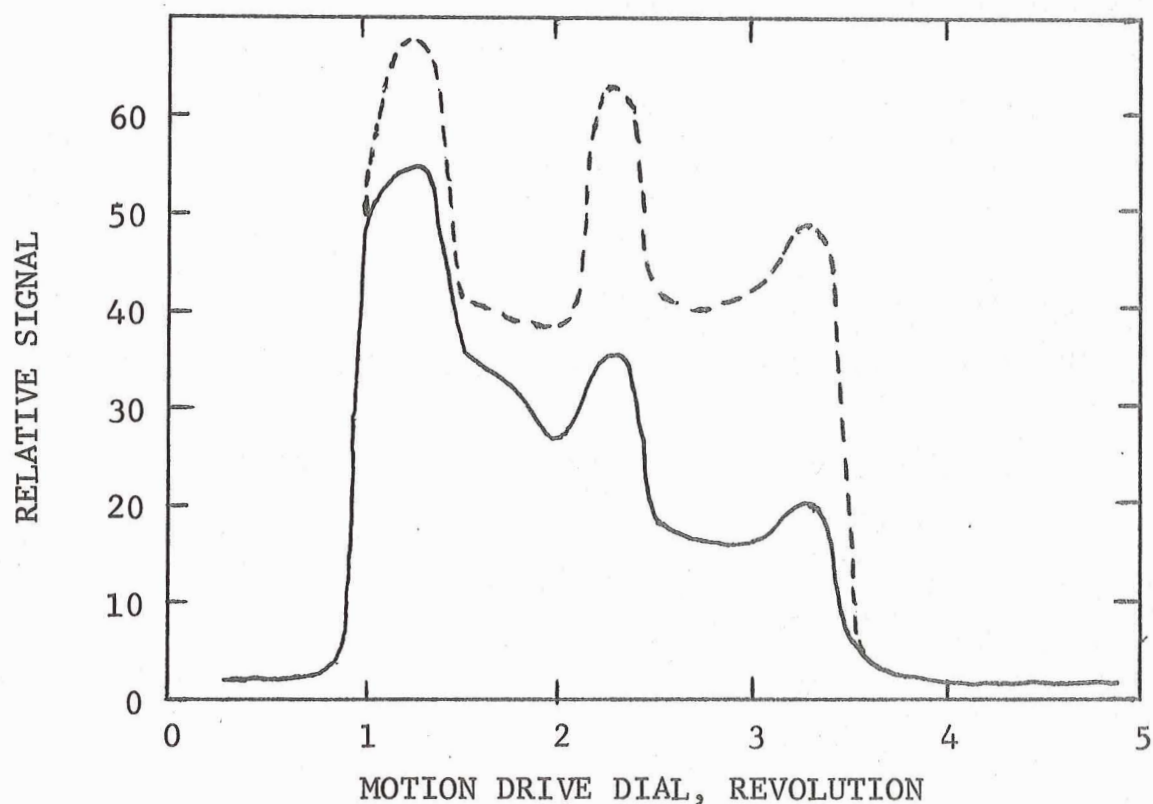


(b) Scan of Element UDT 1-B, UDT 1-A Open.

FIGURE 22. DETECTOR SCANS BEHIND 0.25mm WIDE EXIT SLIT WITH 1215.7 Å RADIATION. ONE DIAL REVOLUTION EQUALS A DETECTOR MOTION OF 1.26mm. (RUN 39).



(a) Scan of Element UDT 1-A, Element UDT 1-B Grounded.
MOTION DRIVE DIAL, REVOLUTION



(b) Scan of Element UDT 1-B, Solid Line for Element UDT 1-A Grounded and Dashed for UDT 1-A Open.

FIGURE 23. DETECTOR SCANS BEHIND 0.25mm WIDE EXIT SLIT WITH 584.3 Å RADIATION. ONE DIAL REVOLUTION EQUALS A DETECTOR MOTION OF 1.26mm. (RUN 39).

when the other element is left open. The average crosstalk for the grounded case is approximately 37%. This unexpectedly high level of crosstalk is probably due to operation with vacuum UV radiation since the rated crosstalk for visible light is less than 10% and normally about 5%. A considerable reduction in the UV crosstalk might be possible by designing a detector with silicon having shorter carrier lifetimes.

The other unexpected phenomena was the existence of a central signal peak during the position scan. This corresponds to the location where the vacuum UV photons are incident on the detector region between the two surface electrodes. This can be explained by the absence of a metal film to absorb or reflect the radiation, permitting more of the photons to reach the p-n junction depletion region and create a larger number of charge pairs. These carriers must then move to the film electrode surface for collection. The same phenomena probably occurs at the outer edges of the electrode areas and accounts for the rapid rise in signal and the two outside peaks. For ordinary operation with visible light the photons easily penetrate the gold layer and probably form charge pairs deeper in the material and are collected mainly in the areas under the electrodes.

The other detector types tested, such as the Fairchild FPM 100 and 200, consisted of discrete elements which could be combined into an array by close physical packing. Thus, with these units, crosstalk in a spectrometer could occur only in the electronics external to the devices themselves.

C. Fatigue and Memory Effects

Since the contemplated reentry spectrometer is only expected to be recording data for 80 seconds, the short term fatigue of a detector when exposed to vacuum UV radiation must be known. Measurements were made both by moving the detector into the photon beam and by turning the beam on and off with an externally operated shutter plate in the detector chamber. Thus, fatigue measurements could be made without varying the UV lamp or spectrometer settings.

The only solid state detector which showed no measurable fatigue was the Fairchild FPM 100 phototransistor. The reason for this performance is unknown and the devices tested may have been from an unusual fabrication lot.

The UDT-1 detector had fatigue periods where the signal dropped 85% in the first 5 minutes and considerably longer memory periods. Exact fatigue figures were difficult to obtain due to the long recovery times. Figures 24 and 25 contain some of the measurement results with the UDT-1 detector for 584.3 and 1215.7 Å radiation. Figure 24 shows the signal variation over an initial 25 min. exposure, then 20 minutes of recovery, another 3 min. exposure, followed by a 17.5 hour recovery period and a final 45 min. exposure. During this test the only system adjustment was the lowering of a shutter into the monochromator beam and the shutting down of the UV lamp during the 17.5 hour interval. The short term fatigue of two areas on the same detector element under 584.3 Å radiation is presented in Figure 25.

The fatigue time constant of the Fairchild FPM 200 photodiode was much shorter than the UDT-1 photodiode as can be seen in Figure 26. The FPM 200 undergoes rapid fatigue in the first 30 seconds and then reaches a plateau. Its recovery period, however, is longer than 10 min. which is the dashed portion of one curve in Figure 26,A. Recovery for the UDT-1 detector is about the same order as evidenced by Figure 26,B. Thus, the memory period for these detectors appears to be on the order of many hours to possibly days.

Since long time interval fatigue and memory studies require that the lamp be shut down, restarted, and stabilized to its previous output, these measurements can be quite lengthy. Also rapid fatigue rates made the sensitivity and NEP measurements very difficult. Due to the usual presence of fatigue, readings were taken when the detector output stabilized. Such problems were also present during the measurements by Tuzzolino with the University of Chicago detectors.

Possible methods of fatigue reduction were not explored, but they might consist of employing higher reverse bias voltages or pre-exposing the detectors to a light mounted in the spectrometer chamber. Since the FPM 100 phototransistor exhibited no fatigue this detector can be considered as a backup should the fatigue problem prove too difficult.

During the measurement period the relative quantum efficiency of the sodium salicylate coated photomultiplier tube declined as shown in Figure 27. This demonstrates the calibration problem that would be encountered if the phosphor were used as a wavelength shifter for a detector array in a reentry spectrometer. Since the phosphor coated PM tube was calibrated by the ion chamber for each data run on the laboratory system this problem was eliminated.

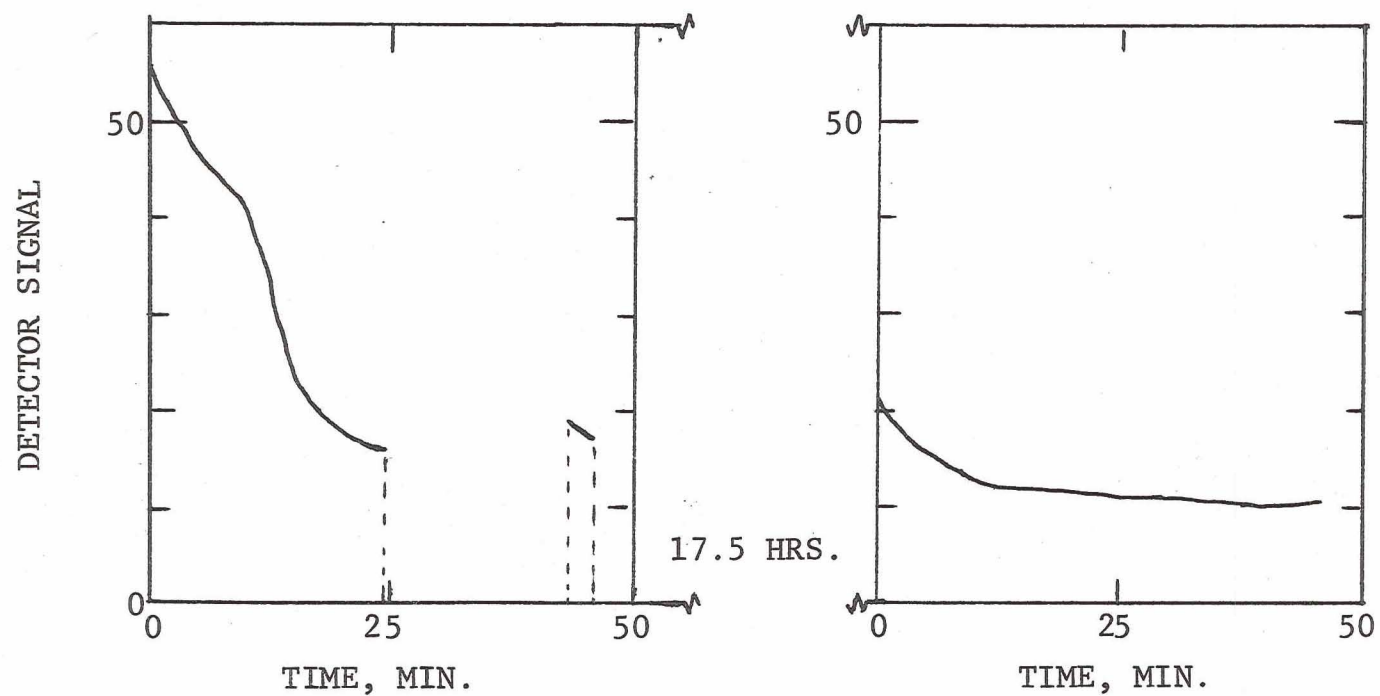
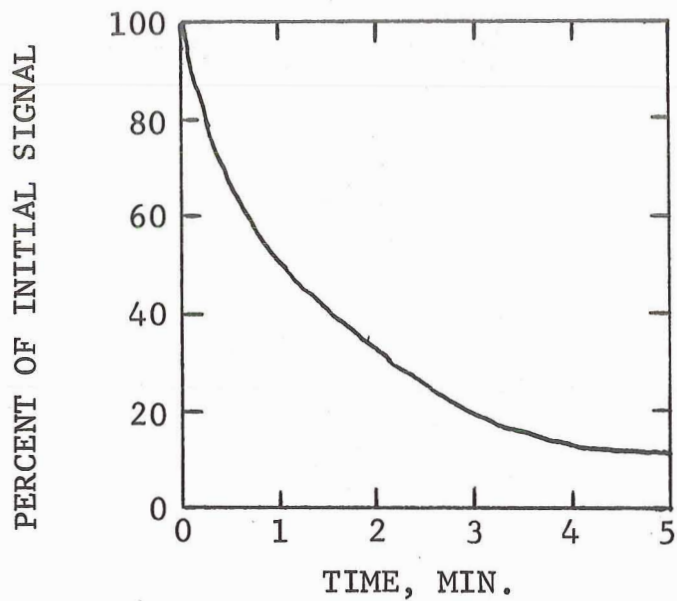
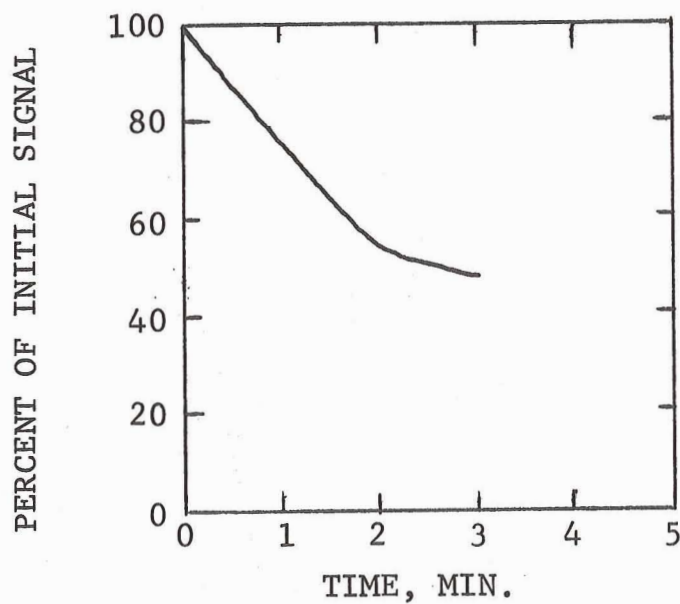


FIGURE 24. FATIGUE MEASUREMENT ON UDT-1-B FOR 1215.7 Å RADIATION.
ELEMENT 1-A LEFT OPEN. (RUN 35 and 36)

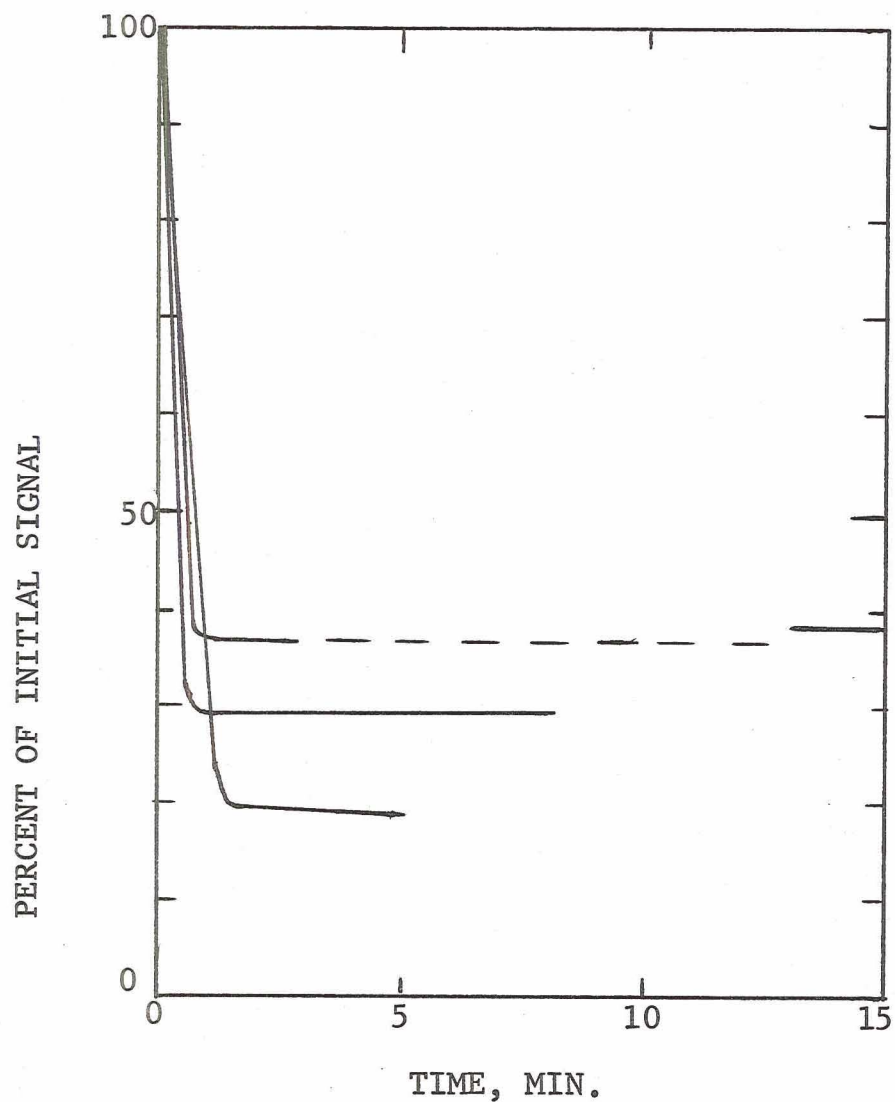


(a) Initial Area Of Detector

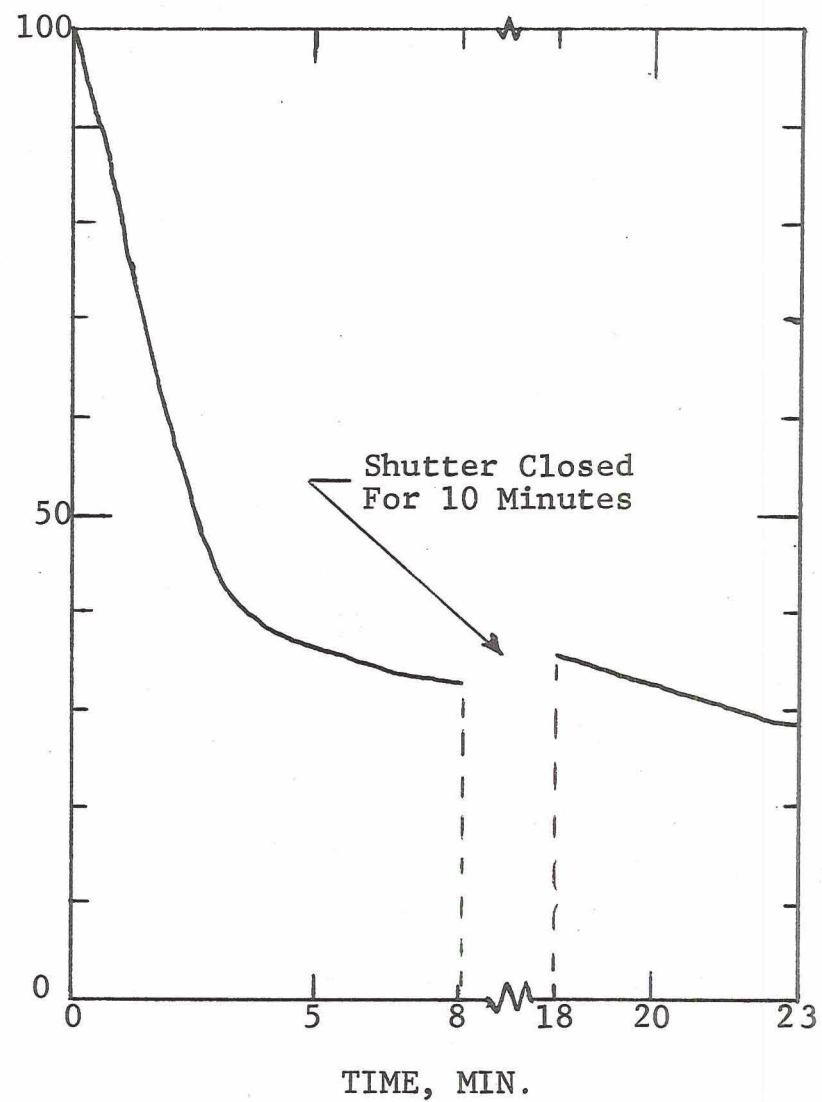


(b) Another Area On The Same Detector

FIGURE 25. FATIGUE MEASUREMENTS AT TWO SPOTS ON THE UDT 1-B DETECTOR ELEMENT WITH 584.3 Å RADIATION. ELEMENT UDT 1-A GROUNDED. (RUN 39).



(a) Fairchild FPM200 Photodiode



(b) UDT 1-A Photodiode

FIGURE 26. FATIGUE TESTS FOR 1215 Å RADIATION. (RUN 38).

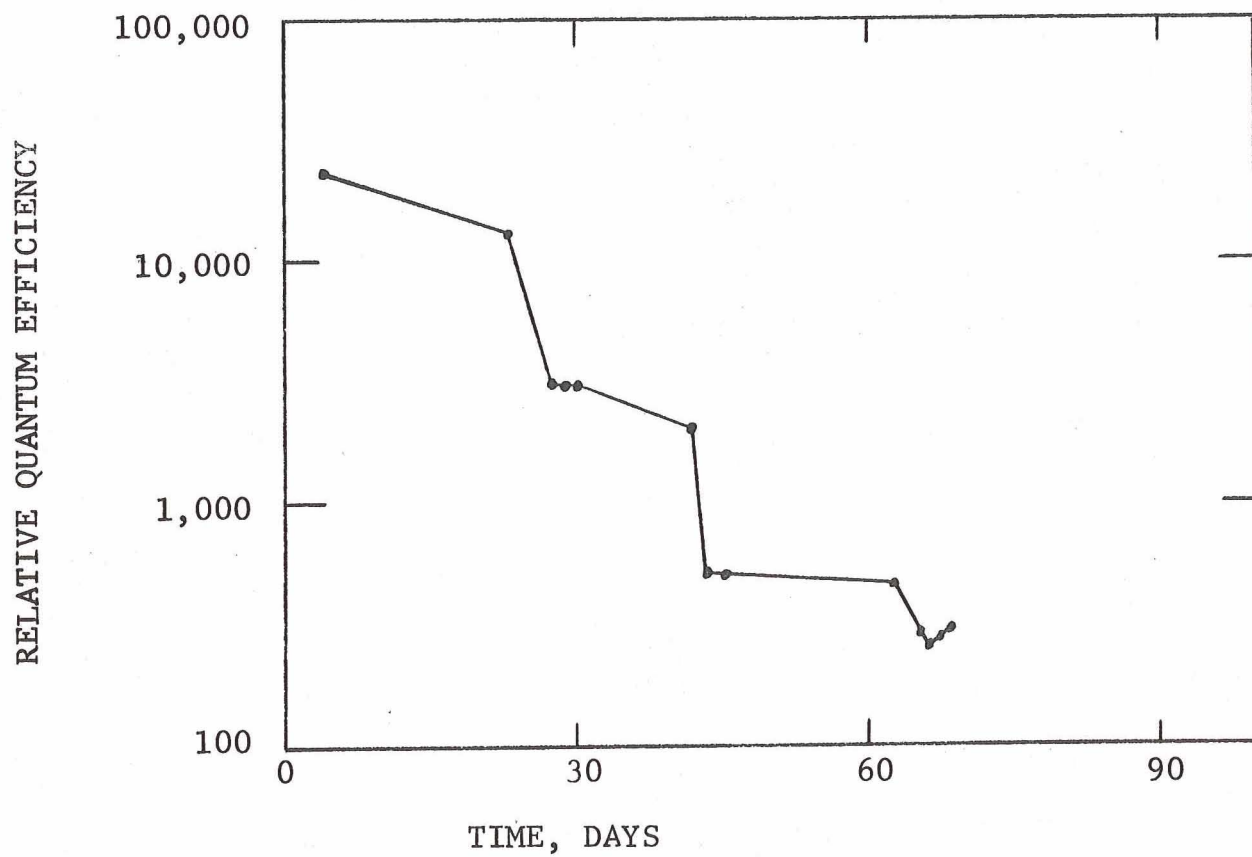


FIGURE 27. DECLINE IN RELATIVE QUANTUM EFFICIENCY
OF THE SODIUM SALICYLATE COATED PM TUBE.

D. Temperature Effects

Changes in the temperature of solid state devices will alter the generation rate and mobility of carriers, thereby increasing the dark or reverse current and its associated noise. The measured variation of dark current with temperature for the various detectors is given in Figure 28. The generation-recombination (g-r) noise is dependent on the dark (reverse) current and further described in the following chapter on noise considerations. The g-r noise values corresponding to the detector dark currents at 22° C are presented in Table 4 and can be calculated from the dark current corresponding to a specific temperature by

$$I_{g-r} = \sqrt{2 e I_{\text{dark}} \Delta f}$$

where e = electronic charge
 Δf = frequency bandwidth.

TABLE 4. DETECTOR DARK CURRENT AND G-R NOISE

Temp. 22°C.	$\Delta f = 10 \text{ Hz.}$	$f = 150 \text{ Hz.}$
DETECTOR	$I_{\text{DARK}} (\text{AMP})$	$I_{g-r} (\text{AMP})$
UDT-1	1.5×10^{-7}	7×10^{-13}
UDT-2	2.0×10^{-7}	8×10^{-13}
U of C	2.5×10^{-7}	9×10^{-13}
FPM 100	5.0×10^{-10}	4×10^{-14}
FPM 200	1.3×10^{-10}	2.1×10^{-14}
HPA 4204	4.6×10^{-11}	1.2×10^{-14}
SnO (-7V)	1.0×10^{-11}	5.7×10^{-15}
(-300V)	8.0×10^{-8}	5.1×10^{-13}

The effect of increased detector temperature could be seen as an increase in noise during experimental runs. Figure 29 shows the detector noise, because of a thermal lag, reaching a peak value slightly after the maximum temperature was measured with the thermal resistance sensor.

Since diffusion processes have been used in the fabrication of several devices, extended high temperature operation above 200° C could change the detector properties. Short heat pulses should not be extremely injurious to the detector since the melting point of silicon is 1420° C and the diffusion temperature is about 800° C.¹³

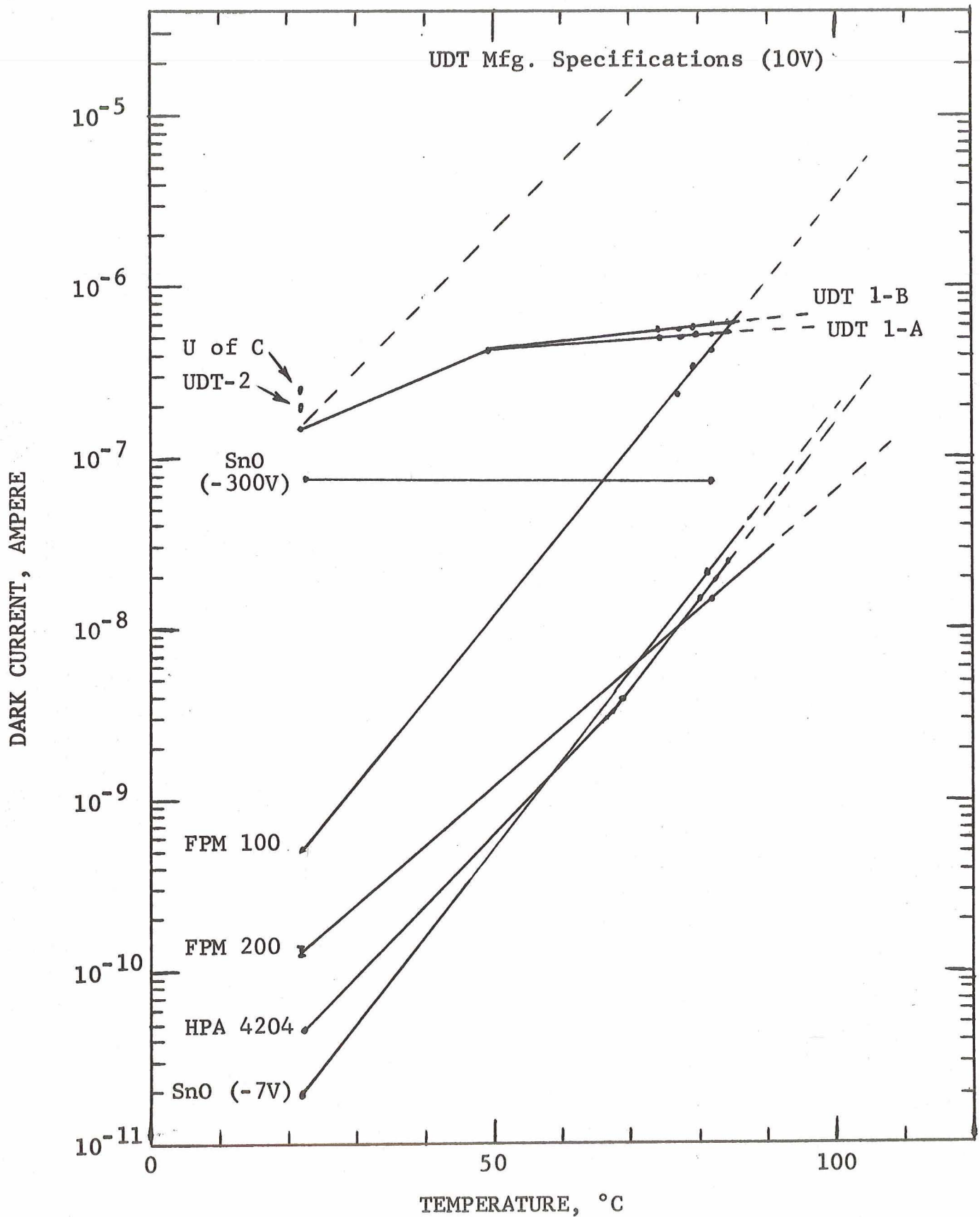
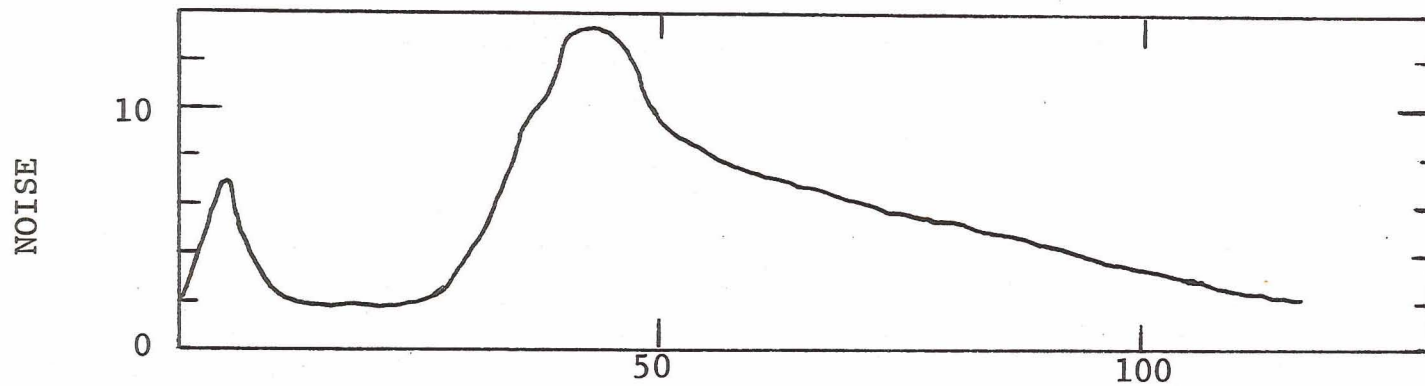
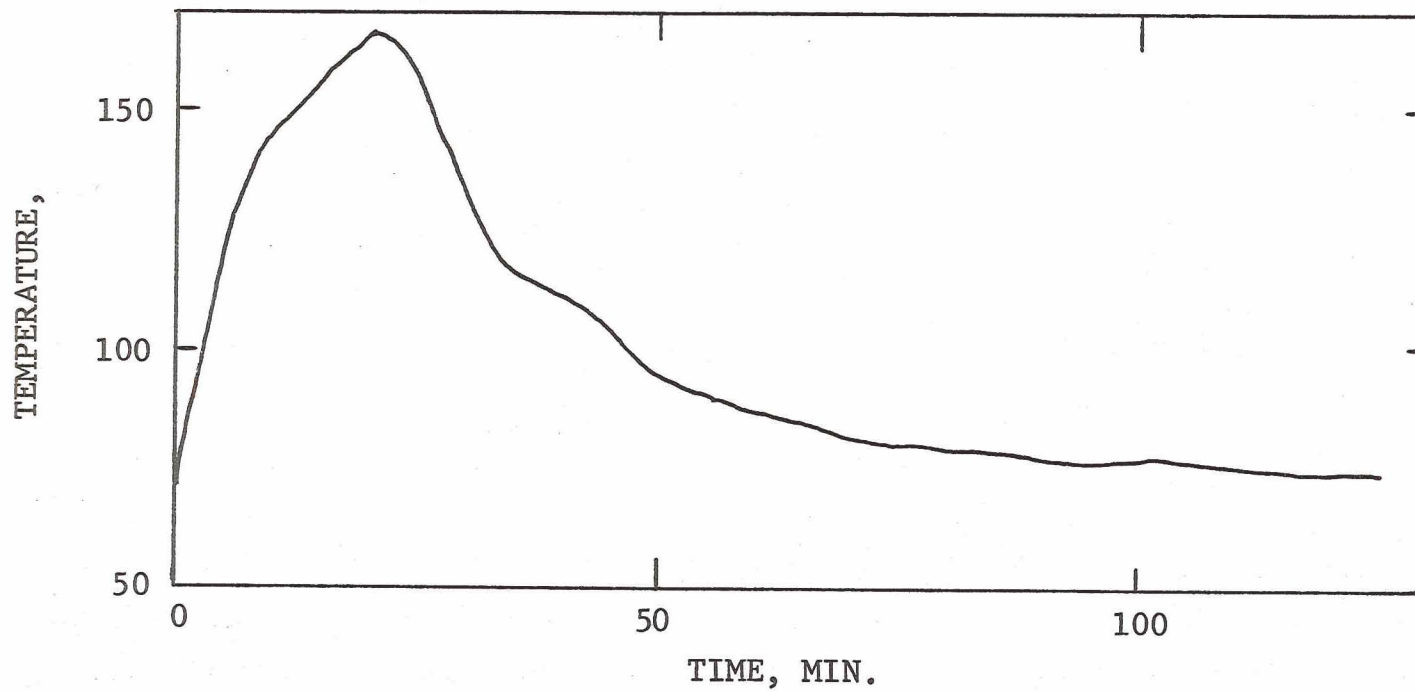


FIGURE 28. REVERSE CURRENT AS A FUNCTION OF DETECTOR TEMPERATURE. BIAS IS 7V EXCEPT WHERE NOTED. (RUN 38).



(a) Detector Noise During Temperature Run.



(b) Temperature Variation With Time.

FIGURE 29. NOISE VARIATION WITH TEMPERATURE IN THE UDT 1-B PHOTODIODE. (RUN 37).

E. Long Term Stability

During the 3.5 month period over which detector measurements were made no changes were observed in the spectral response or sensitivity of the devices, aside from the previously mentioned fatigue. The stability and resistance to atmospheric contamination and aging was demonstrated by the University of Chicago gold surface barrier detector which is approximately 6 years old and still responded to vacuum UV radiation with its original sensitivity. This does not mean that all silicon devices are immune to changes, but does demonstrate the long lifetime of the surface barrier type construction for operation within certain environmental limits.

F. Frequency Response

The rated frequency response for the solid state detectors is presented in Table 5.

TABLE 5. RATED FREQUENCY RESPONSE

Values obtained from manufacturer's specifications.

<u>DETECTOR</u>	<u>RESPONSE TIME, SEC.</u>
UDT PIN-Spot/2	10^{-8}
Fairchild FPM 100	3×10^{-6}
Fairchild FPM 200	3×10^{-6}
Hewlett Packard 4204	10^{-9}

All the times are considerably shorter than that required for the 150 Hz photon beam modulation frequency and should be quite adequate for any solid state scanning array. For low S/N operation the noise-limited frequency response must also be considered. This is discussed in the following chapter.

G. Other Parameters

1. Reverse Bias Voltage

The reverse bias voltage of all solid state junction detectors was 7V during this study. During operation with a particular detector it is possible to vary the bias voltage within a certain range and maintain the same sensitivity. The bias voltage range and the maximum voltages as specified by the manufacturers are presented in Table 6.

TABLE 6. REVERSE BIAS VOLTAGE RANGE

<u>DETECTOR</u>	<u>RANGE, VOLTS</u>	<u>MAXIMUM, VOLTS</u>
UDT PIN-Spot/2	5-100	---
Fairchild FPM 100 *	5- 40	40
Fairchild FPM 200	5-100	100
Hewlett Packard 4204	3- 20	20

* collector-emitter ratings.

Increasing the bias voltage usually results in an increase in the dark current and the depletion layer thickness. The advantage of increasing the depletion layer, which is the region over which the photon generated charge pairs are collected, depends mainly on the structure of the particular detector. Devices such as the surface barrier detectors where the depletion layer is virtually at the surface may experience no increase in sensitivity with high bias voltages since the depletion layer depth may only be increased downward into the device. This is due to the limited penetration of the vacuum UV radiation in silicon as presented in Figure 30.

2. Spatial Resolution

Detectors with a number of elements on the same chip can be made with masking techniques to achieve upwards of 100 elements per inch. As previously mentioned the limitations of crosstalk and variation in sensitivity must be considered. The United Detector Technology PIN-Spot/2 detectors represented an array of elements which had their centers separated by 1.25 mm. Discrete devices where the silicon chips are separated but still inside the same container can be custom fabricated to below one mm element widths while the completely discrete detectors such as the Fairchild FPM 100 can be placed in their own cans on 2 mm separation between centers.

VII. NOISE CONSIDERATIONS

In order to determine the minimum detectable power and the noise-limited frequency response of the various detectors, the sources of noise in the measuring system must be known.

A. Noise Sources

In the measurement system the four main sources of noise are; Johnson or thermal, generation-recombination, modulation 1/f, and environmental noise.

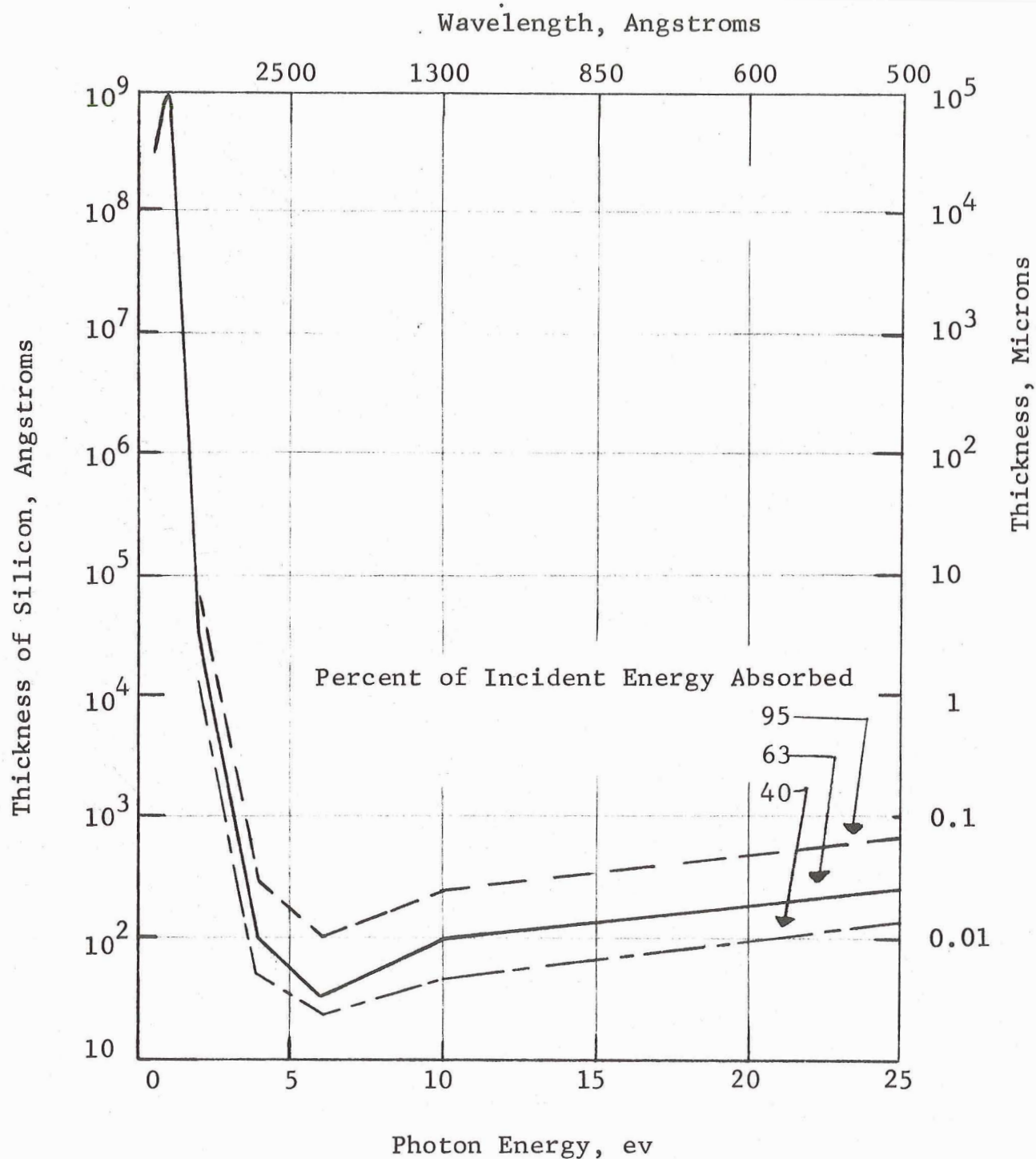


Figure 30. PENETRATION OF RADIATION IN SILICON.

(From J. Tauc, Progress in Semiconductors, Ed. A. F. Gibson and R. E. Burgess, Temple Press, London, 1965 p. 114, and T. S. Moss, Optical Properties of Semi-Conductors, Butterworth, London, 1959, p. 116, 121.)

1. Johnson or Thermal Noise

Johnson noise is caused by the random thermal motion of electrons through a conductor. This motion is interrupted by electron collisions with the molecules of the conductor. Although the mean current due to all electrons is zero, there is a statistical variance in the instantaneous current. This variance is termed Johnson noise and its rms current value is equal to

$$i_t = \sqrt{\frac{4 k T \Delta f}{R}}$$

where k = Boltzmann's constant
 T = absolute temperature
 R = resistance
 Δf = bandwidth, Hz.

At room temperature (290°K),

$$i_t = 0.13 \sqrt{\frac{\Delta f}{R}}, \text{ picoamp}$$

where R = resistance in megohms.

As an example, a one megohm resistor has a noise current of

$$i_t = 0.13 \sqrt{\Delta f}, \text{ picoamp.}$$

Johnson noise is white; that is, the mean square current is independent of frequency, and the noise spectrum is flat.

2. Generation-Recombination (g-r) Noise

In a semiconductor, electron-hole pairs are generated by the absorption of photons or by thermal motion (dark current). Fluctuations in the rate at which these charge carriers are generated and recombined cause variations in the conductivity of the material, thereby giving rise to g-r noise. It is the semiconductor counterpart of vacuum tube shot noise, but is larger by a factor of two because there are two processes involved.

The noise power spectrum of g-r noise is flat from low frequencies up to a frequency that is approximately equal to the inverse of the free carrier lifetime. Above this frequency the power spectrum falls off as the inverse-square power of

the frequency. The frequency dependence of the rms g-r noise current can be expressed as

$$i_{g-r} = \sqrt{\frac{4 e I \Delta f}{1 + (2\pi f \tau)^2}}$$

where e = electronic charge

I = dark current mean photocurrent

Δf = bandwidth

f = frequency

τ = free carrier lifetime

At low frequencies $2\pi f \tau \ll 1$ and the root-mean-square g-r noise current is given by

$$\begin{aligned} i_{g-r} &= \sqrt{4 e I \Delta f} \\ &= 0.0008 \sqrt{I \Delta f}, \text{ picoamp} \end{aligned}$$

where I = mean junction current in picoamperes

Δf = bandwidth in Hz.

Thus, for a typical dark current of 0.1 microamp,

$$i_{g-r} = 0.25 \sqrt{\Delta f}, \text{ picoamp.}$$

3. Modulation (1/f) Noise

In the frequency region below 100 Hz, modulation noise usually dominates over the Johnson and g-r components. This noise is thought to result from imperfect surface conditions in solid state components and elements such as carbon-composition resistors. The exact physical mechanism is not well understood, but the noise appears as conductivity fluctuations. Pink noise is a generic term applied to ideal $1/f$ noise where the noise voltage is exactly proportional to $\sqrt{1/f}$. The rms modulation noise current is described by

$$i_f = \sqrt{K I \Delta f / f^\alpha}, \text{ amp}$$

where K = constant

I = mean junction current

Δf = bandwidth, Hz

f = frequency, Hz

α = constant dependent on type of device.

Generally, α varies between 0.8 and 1.5

4. Environmental Noise

These are disturbances which effect measurements, but can in principle be reduced to an arbitrarily small value. The principal contribution occurs at 60 hertz and higher harmonics, from power lines, motors, and instruments. Temperature changes, earth and building vibrations, and other induced fluctuations are also noise sources in this category. In most cases, apart from the power line frequencies, the region between 1 and 10^6 Hz appears to be comparatively free of environmental noise.

5. Total Noise

The rms noise voltages or currents from essentially uncorrelated sources are combined by computing the square root of the sum of their squares. Thus, larger quantities are emphasized and the smaller are suppressed. Combining the previous noise sources produces a noise power spectrum similar to Figure 31. The magnitude of the $1/f$ noise and the charge-carrier lifetime of the g-r noise determine the location and extent of the "hump" in the spectrum.

B. Noise Measurements

1. Silicon Reversed-Bias Photodiodes

In order to discuss the measurement of noise in silicon reversed-bias photodiodes a brief operational description is included here. Such a device is shown schematically in Figure 32. The photocurrent, I_p , is the same for any impedance presented. The output voltage V_o is given by

$$V_o = \frac{I_p R_L}{R_c + R_L} \left[\frac{1}{R_J} + \frac{1}{R_c + R_L} \right]^{-1}.$$

Since $R_c \ll R_L \ll R_J$, the above reduces to

$$V_o = I_p R_L.$$

The diode capacitance C_d determines the high-frequency response of the device, and we can write

$$V_o(f) = I_p R_L [1 + (2\pi f R_L C_d)^2]^{-1}.$$

However, in the frequency range of interest (below 10,000 Hz) the frequency dependence can be neglected. Also in this analysis and subsequent measurements, the load resistor is considered to be a part of the detector.

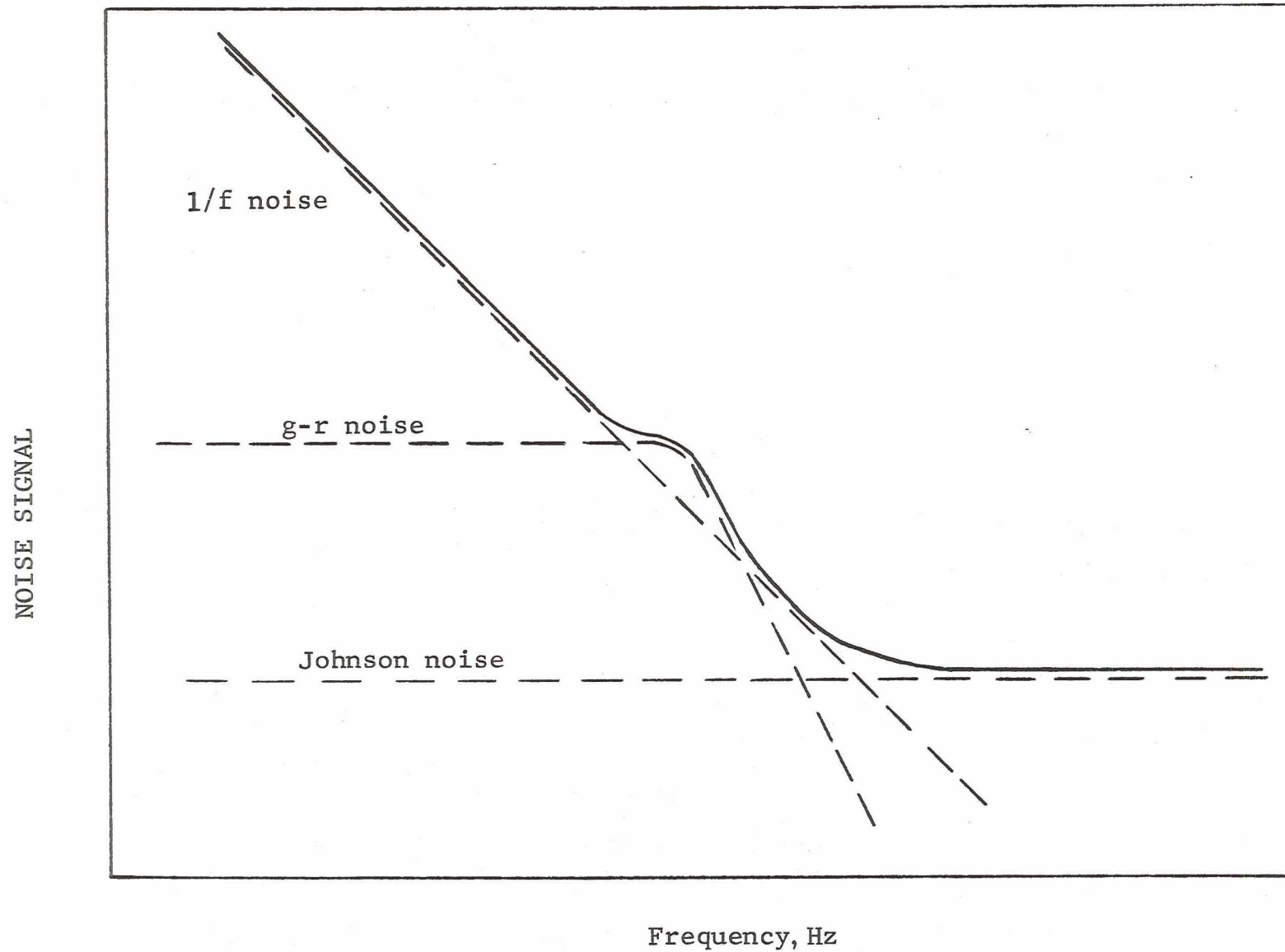


Figure 31. IDEAL DIODE NOISE SPECTRUM

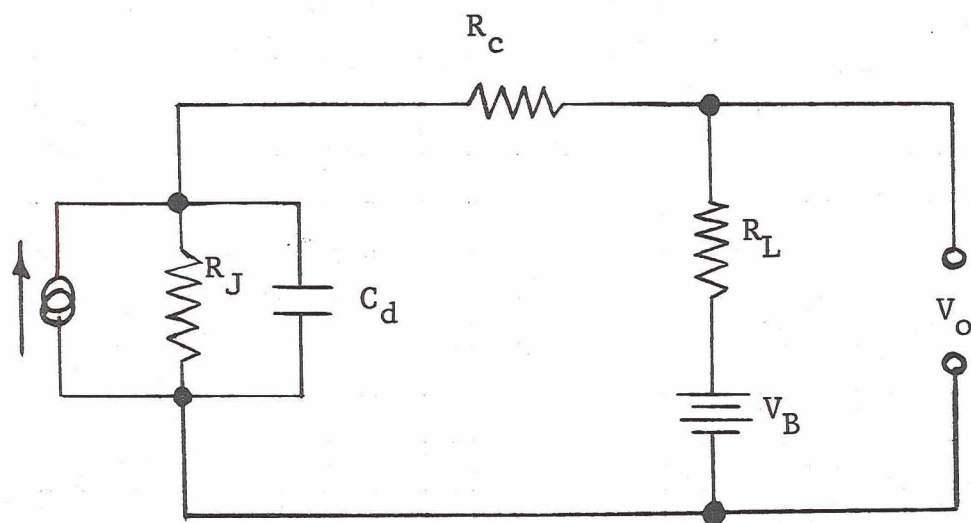


FIGURE 32 EQUIVALENT CIRCUIT OF A SILICON PHOTODIODE

2. Johnson Noise

For a reversed-bias photodiode the load resistance is much smaller than the junction resistance, and therefore, the Johnson noise will be determined by the value of R_L . Two values of R_L were used, 1.0×10^6 ohm and 1.2×10^7 ohm. The corresponding values of Johnson noise (for $\Delta f = 1$ Hz.) are

$$i_t = 0.13 \text{ picoamp, for } R_L = 1.0 \text{ megohm, and}$$

$$i_t = 0.035 \text{ picoamp, for } R_L = 12 \text{ megohm.}$$

3. G-R Noise and Dark Current

In order to obtain the magnitude of the g-r noise term it is necessary to measure the dark current.

Two detectors were chosen for the analysis. Both were silicon surface-barrier photodiodes (a PIN-Spot/2 obtained commercially from United Detector Technology, and a No. 1490 from the University of Chicago). Each was biased with 7.0 volts and used the same load resistor-preamplifier combination.

The dark current of the two diodes was determined by measuring the output voltage V_o with:

(1) an oscilloscope with 1 megohm input

(2) an electronic voltmeter with 10^9 ohm input.

Both determinations gave the following values of dark current, I_d :

$$(I_d)_{UDT} = 0.33 \text{ picoamp}$$

$$(I_d)_{UofC} = 0.13 \text{ picoamp.}$$

The corresponding values of the rms g-r noise are

$$i_{g-r} = 0.42 \text{ picoamp, UDT}$$

$$i_{g-r} = 0.64 \text{ picoamp, U of C.}$$

4. Detector-Preamplifier Interface

Before the noise power spectrum can be determined the effect of a large load resistance on the preamplifier input impedance must be analyzed. Consequently, the frequency response of the preamplifier must be measured. The preamplifier used to amplify the noise voltages prior to measurement was a Tektronix type 122 which was specially modified to perform low-frequency noise analyses.

The input circuitry of the Tektronix 122 includes a ten megohm resistor and a 50 picofarad capacitance between signal and ground. In addition, a 0.01 microfarad capacitor has been added to the signal path to provide a.c. coupling. Since only four inches of coaxial cabling is used, the cable capacitance (10 picofarads) can be neglected. The complete input circuit is shown in Figure 33.

In order to determine the frequency response of the input circuit two calculations must be performed. First, the frequency-dependent impedance, β , which is presented to the current source (photodiode) must be calculated. And second, the fraction, α , of the voltage developed across this impedance which is incident on the preamplifier gain stages must be calculated.

The effective impedance is determined by the parallel combination of the load resistance, R_L , and the preamplifier input impedance, X . The dependence of X on frequency can be expressed as

$$X(f) = X_1(f) + R'(f),$$

where R' is the parallel combination of C_2 and R_2 ; i.e.,

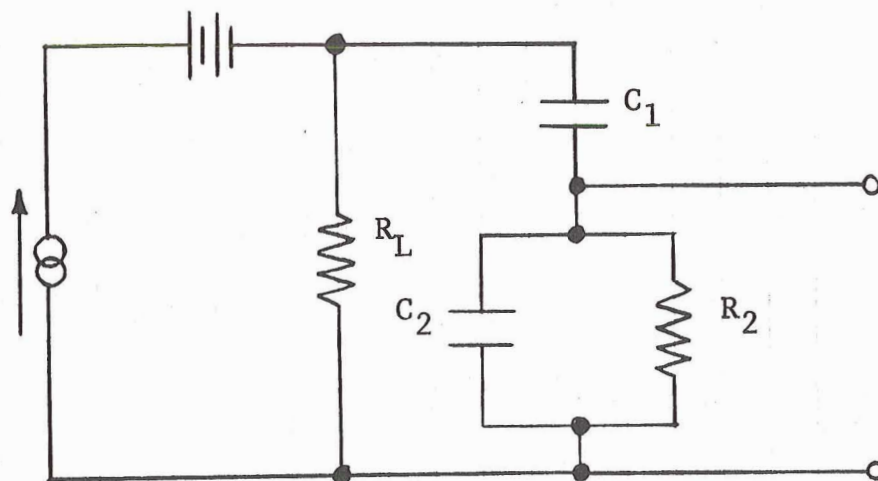
$$R'(f) = \left[\frac{1}{X_2} + \frac{1}{R_2} \right]^{-1} = \frac{R_2}{1 + 2\pi f R_2 C_2};$$

Thus $X(f)$ is

$$\begin{aligned} X(f) &= \frac{1}{2\pi f C_1} + \frac{R_2}{1 + 2\pi f R_2 C_2} \\ &= \frac{1 + 2\pi f R_2 C_2 + 2\pi f R_2 C_1}{2\pi f C_1 (1 + 2\pi f R_2 C_2)}. \end{aligned}$$

But $C_1 \gg C_2$, so

$$X(f) \approx \frac{1 + 2\pi f R_2 C_1}{1 + 2\pi f R_2 C_2} \left(\frac{1}{2\pi f C_1} \right).$$



R_L = Load Resistance
 R_2 = Input Resistance
 C_1 = AC Coupling Capacitance
 C_2 = Input Capacitance
 $X_1 = 1/2\pi fC_1$
 $X_2 = 1/2\pi fC_2$

FIGURE 33. INPUT CIRCUIT FOR NOISE MEASUREMENT

The effective impedance $\beta(f)$ can now be written as

$$\begin{aligned}\beta(f) &= \left[\frac{1}{R_L} + \frac{1}{X(f)} \right]^{-1} \\ &= \left[\frac{1}{R_L} + \frac{1+2\pi f R_2 C_2}{1+2\pi f R_2 C_1} (2\pi f C_1) \right]^{-1}.\end{aligned}$$

The fraction of β which is measured by the preamplifier is

$$\alpha(f) = \frac{R'(f)}{X(f)} \approx \left[1 + \frac{1}{2\pi f R_2 C_1} \right]^{-1}.$$

The frequency response of the preamplifier $T(f)$ is

$$T(f) = \frac{\alpha(f) \beta(f)}{[\alpha(f) \beta(f)]_{\max}},$$

and the normalized noise power spectrum is

$$S(f) \frac{\overline{V^2}}{\Delta f} = \frac{\overline{V_m^2}}{\Delta f} K(f),$$

where $K(f) = T^{-2}(f)$

$\overline{V_m^2}$ = measured mean square voltage.

Table 7 lists the values of K for the following parameters:

$$\begin{aligned}R_L &= 1.0 \text{ megohm} \\ C_1 &= 0.01 \text{ microfarad} \\ C_2 &= 50 \text{ picofarad} \\ R_2 &= 10 \text{ megohm.}\end{aligned}$$

TABLE 7. NOISE MEASUREMENT PARAMETERS

f, Hz	α^{-1}	β^{-1}	K	K'
1	2.6	1.04×10^{-6}	5.5	22.
2	1.8	1.06	2.7	5.4
4	1.4	1.07	1.74	2.4
8	1.2	1.09	1.30	1.30
16	1.10	1.10	1.11	1.11
32	1.05	1.11	1.04	1.04
64	1.03	1.12	1.00	1.00
128	1.01	1.14	1.00	1.00
250	1.01	1.18	1.07	1.07
500	1.00	1.26	1.20	1.20
1000	1.00	1.41	1.52	1.52
2000	1.00	1.73	2.3	2.3
4000	1.00	2.4	4.4	4.4
8000	1.00	3.6	10.	14.
16000	1.00	6.1	28.	55.

The values K' include an additional normalization factor for the noise measurement equipment response.

Table II lists the values of K for the previous parameters with the exception that R_L is 12 megohm.

TABLE 8. NOISE MEASUREMENT PARAMETERS

f , Hz	α^{-1}	β^{-1}	K	K'
1	2.6	1.22×10^{-7}	2.7	11.
2	1.8	1.40	1.66	3.3
4	1.4	1.54	1.26	1.76
8	1.2	1.70	1.05	1.05
16	1.1	1.78	1.00	1.00
32	1.05	1.88	1.03	1.03
64	1.03	2.00	1.10	1.10
128	1.01	2.2	1.26	1.26
250	1.01	2.6	1.79	1.79
500	1.00	3.4	3.1	3.1
1000	1.00	4.9	6.3	6.3
2000	1.00	8.1	17.	17.
4000	1.00	1.5×10^{-6}	61.	61.
8000	1.00	2.7	190.	270.
16000	1.00	5.2	710.	1400.

5. Noise Power Spectra

Noise power spectra were determined for both the UDT and the University of Chicago detectors. In addition, thermal noise spectra were obtained for both the one megohm and the twelve megohm load resistors to check the normalization accuracy.

The noise measurement is shown schematically in Figure 34. Frequencies were chosen between 5 and 10,000 Hz, and the mean-square voltages measured were divided by the bandwidth to obtain normalized power spectra.

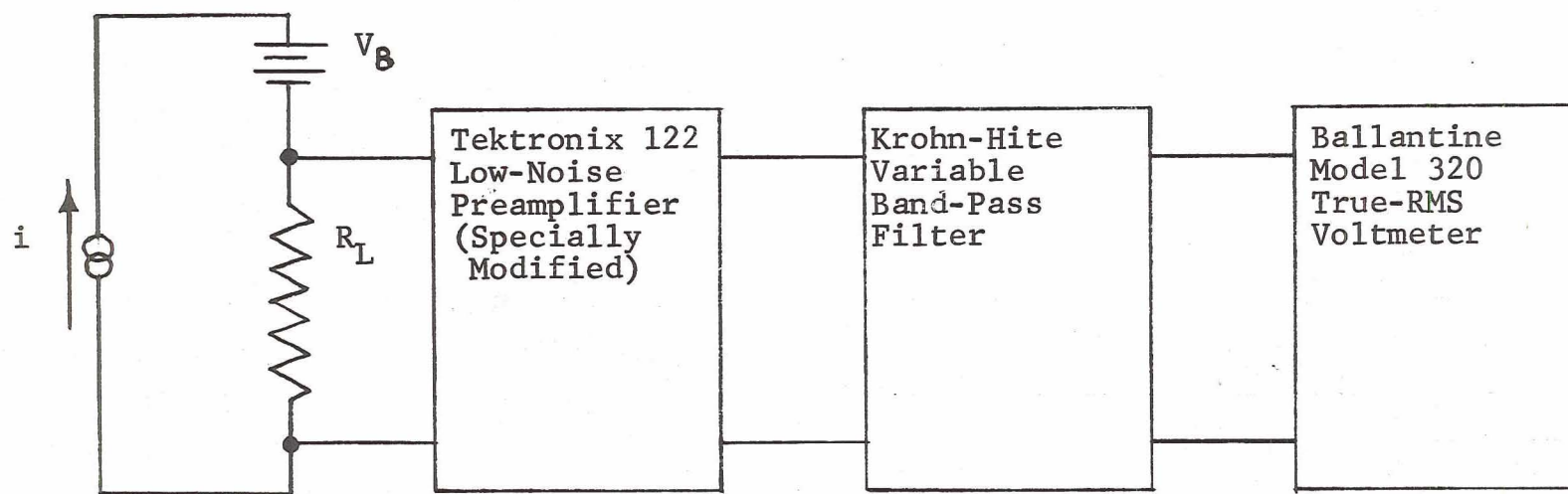


FIGURE 34 NOISE MEASUREMENT SYSTEM

To convert the measured data to units of current referred to the detector, both the gain of the electronic instrumentation and the preamplifier input impedance must be considered. The gain of the electronics is just that of the preamplifier (i.e., one thousand); thus, the conversion is

$$\frac{\overline{V^2}}{\Delta f} = \frac{\overline{V_m^2}}{\Delta f} K'(f) \times 10^6$$

and

$$\frac{\overline{i^2}}{\Delta f} = \frac{\overline{V^2}}{\Delta f} \left[\alpha(f) \beta(f) \right]_{\max}^{-2}$$

alternatively, this may be written as

$$\frac{\overline{i^2}}{\Delta f} = \frac{\overline{V_m^2}}{\Delta f} \cdot \left[\alpha(f) \beta(f) \right]^2.$$

Figure 35 shows the measured noise power spectra of the two photodiodes and the load resistors. The flat power spectra are typical of Johnson noise and indicate that the normalization was successful. Identical results were obtained for the detectors with both load resistors, as would be expected. It can be seen that $1/f$ noise is the dominant diode noise source within the frequency range of the measurements at 150 Hz, the frequency of the tuning fork chopper used in the signal to noise measurements. The noise spectrum indicates noise currents of 1.3×10^{-12} A. These current levels are a factor of 37 above the Johnson noise of the twelve megohm load resistor and equal to the current levels predicted by the NEP. Thus, the detector is limited by the $1/f$ noise at 150 Hz.

It is clearly evident that the NEP of a solid-state detector is strongly dependent upon the frequency. If very low frequency information is to be accurately measured, large signal fluxes must be available or a chopper and lock-in-detector combination must be used.

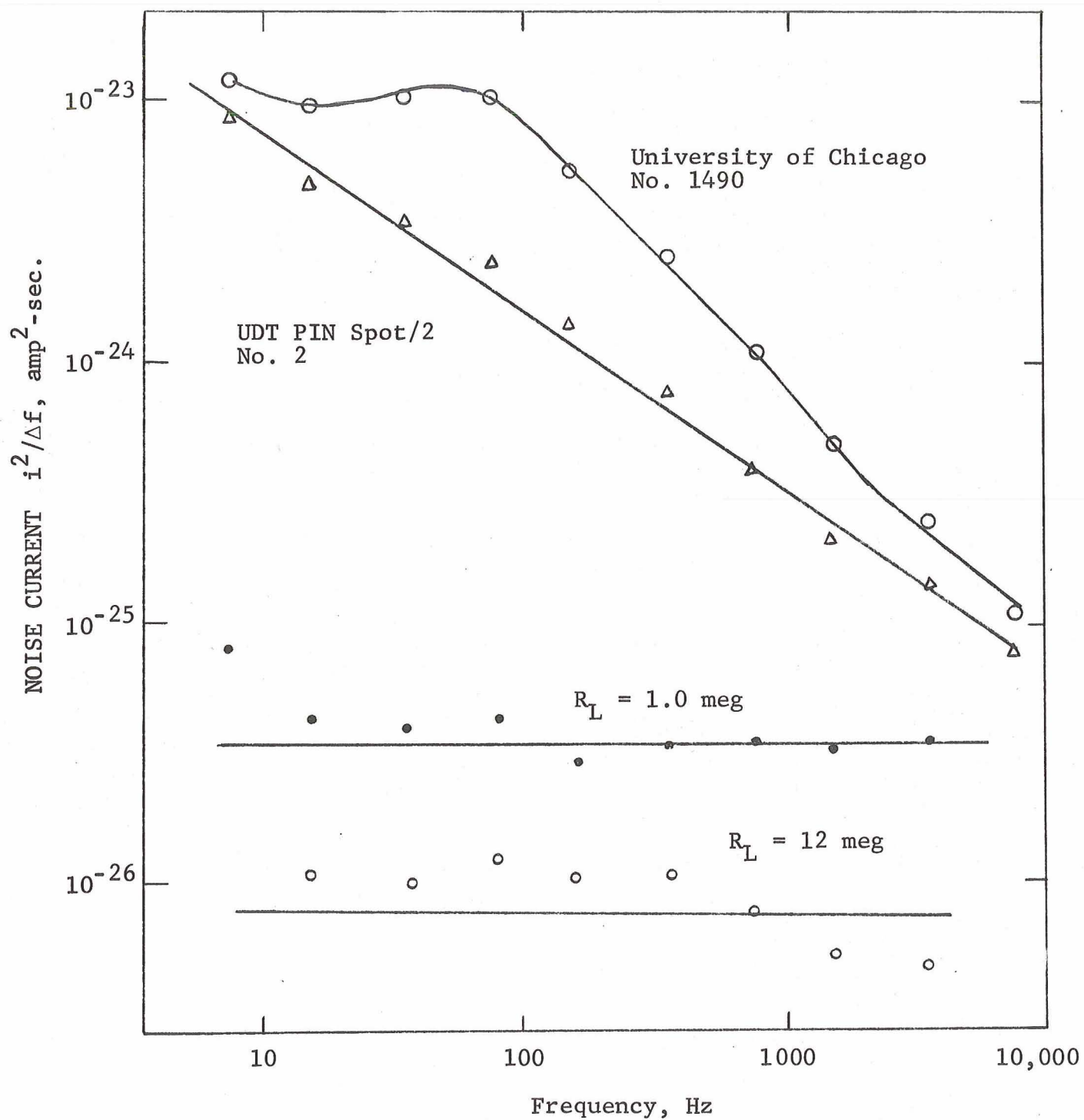


FIGURE 35 MEASURED DIODE NOISE SPECTRUM

VIII. SPECTROMETER DESIGN

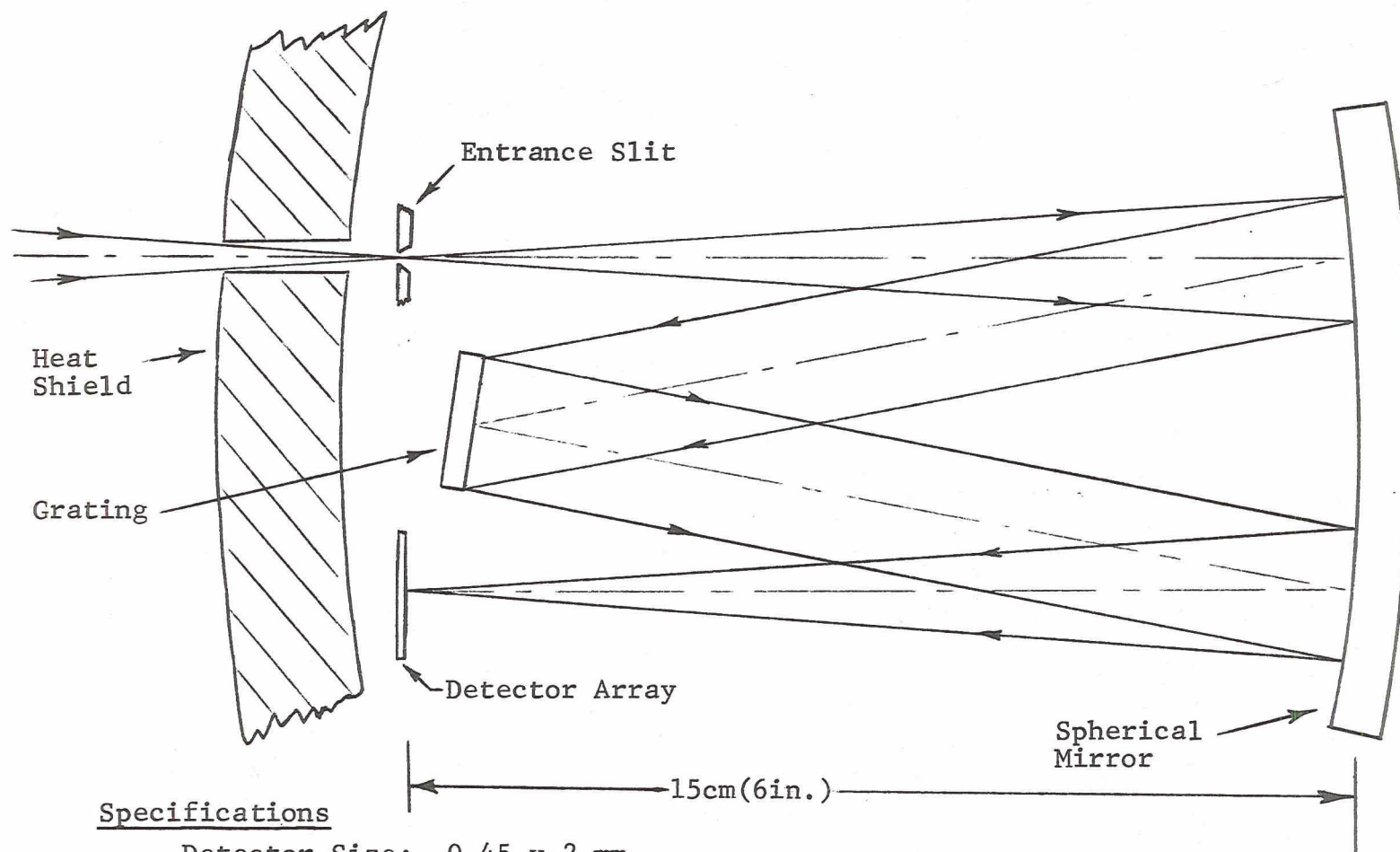
A. Design I: Ebert-Fastie Spectrometer

In order to fulfill mission requirements the spectrometer must have a spectral resolution of 50 Å and cover a spectral range of at least 500 Å to 2000 Å. It would be desirable to have the option of extending the spectral range in the long wavelength direction without extensive alteration of the instrument.

The Ebert-Fastie spectrometer will fulfill these requirements and result in a compact instrument. Other types of instruments can be used and will be briefly discussed later.

The basic Ebert-Fastie design is shown in Figure 36. It consists of an entrance slit, a single concave spherical mirror, a plane diffraction grating and a detector array. Radiant power from the shock front enters the spectrometer cavity through a hole in the heat shield. The opening is 3/16 in. diameter and the heat shield is 3/4 in. thick. The entrance slit is located 1/4 in. behind the heat shield. The geometry of this entrance port limits the solid collection angle of the spectrometer. Hence, the flux collected by the spectrometer is determined by the product of the solid collection angle and the area of the slit. For the Ebert spectrometer the magnification of the system is unity; hence, the size of the entrance slit is determined by the size of the detector element, and the focal length by the resolution requirements. Using these conditions results in a spectrometer with the following specifications:

Detector size:	0.45 wide x 2 mm high
Detector array:	30 elements
Spectral range:	500 Å - 2000 Å
Slit size:	0.45 x 2 mm
Resolution:	50 Å
Focal length of Mirror:	150 mm
Grating ruling:	600 grooves/mm
Grating size:	20 x 20 mm
Grating blaze	1200 Å - 2.4°



Detector Size: 0.45 x 2 mm
 Slit Size: 0.45 x 2 mm
 Resolution: 50 Å
 Mirror F.L.: 150 mm
 Grating Ruling: 600 grooves/mm
 Grating Size: 20 x 20 mm

FIGURE 36. DESIGN I EBERT SPECTROMETER FOR VACUUM UV.

To accept the entire cone of radiation entering the slit requires that the mirror be only 25 mm in height. The entire cavity required by the spectrometer is a rectangular box 175 mm long x 100 mm wide x 25 mm high.

B. Radiant Power

The radiant power per spectral resolution element may be expressed as follows:

$$W_{\Delta\lambda} = N_{\Delta\lambda} A \Omega T \epsilon$$

where $W_{\Delta\lambda}$ = power incident on each detector element (or spectral resolution element)

$N_{\Delta\lambda}$ = radiance of source per spectral resolution element

A = area of slit

Ω = solid angle of collection

T = transmissivity of the spectrometer

ϵ = grating efficiency.

The Ebert spectrometer has a linear wavelength dispersion; that is, the resolution is fixed by the entrance slit width and is a constant 50 Å over the entire spectral range of the instrument. To employ the previous equation for the spectrometer design it will be necessary to convert the radiance values from Chapter II. These values are given in units of watts $\text{cm}^{-2}\text{ster}^{-1}\text{ev}^{-1}$ as a function of ev . The conversion of these values to a plot of watts $\text{cm}^{-2}\text{ster}^{-1}(50\text{\AA})^{-1}$ versus angstroms is shown in Figures 37 and 38 for the adiabatic and nonadiabatic cases, respectively.

The power incident on a detector element for three different wavelengths from the continuum level in both the adiabatic and nonadiabatic cases is shown in Table 9.

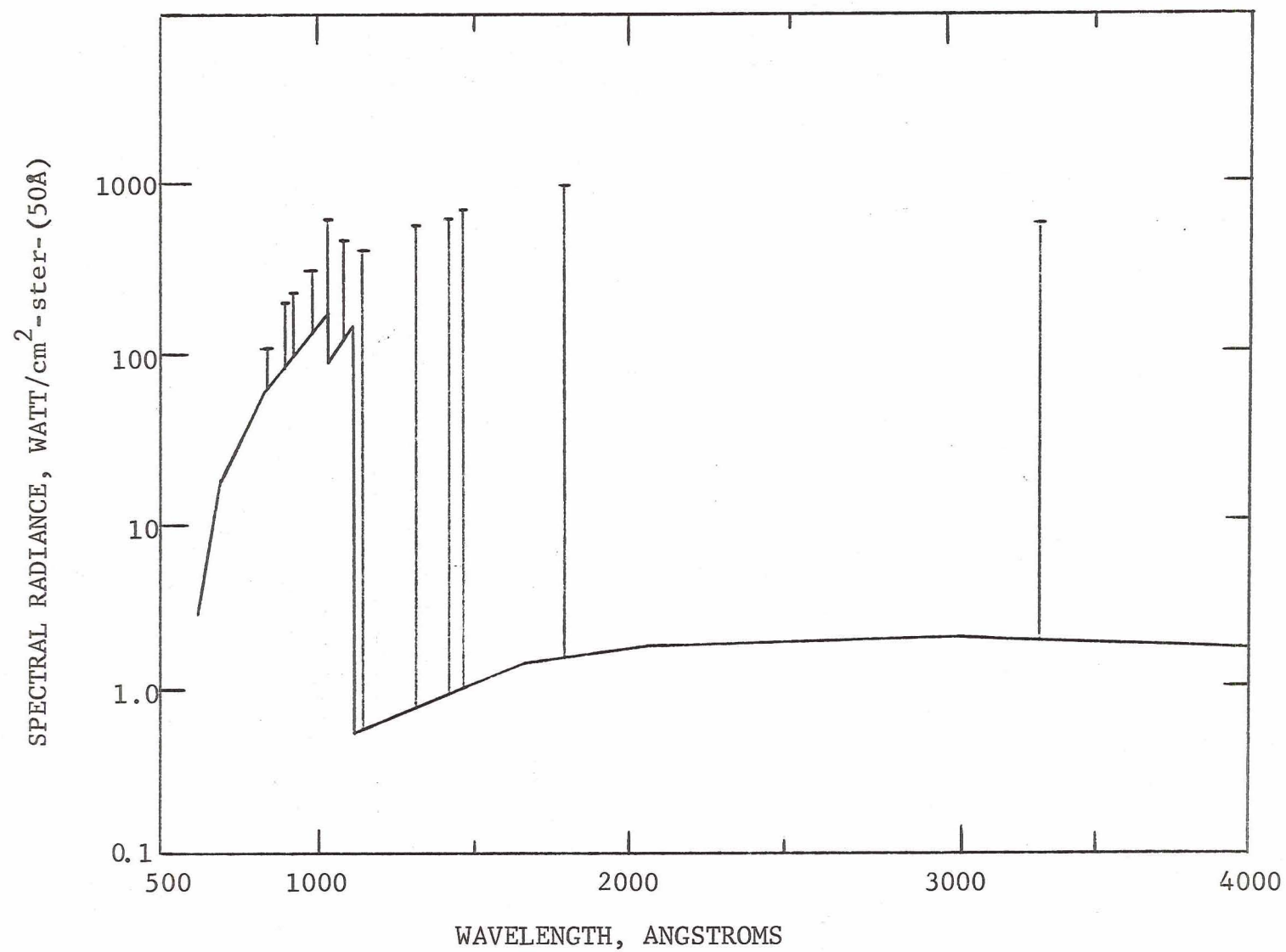


FIGURE 37. SPECTRAL RADIANCE OF BODY, ADIABATIC CASE (9/18/69).

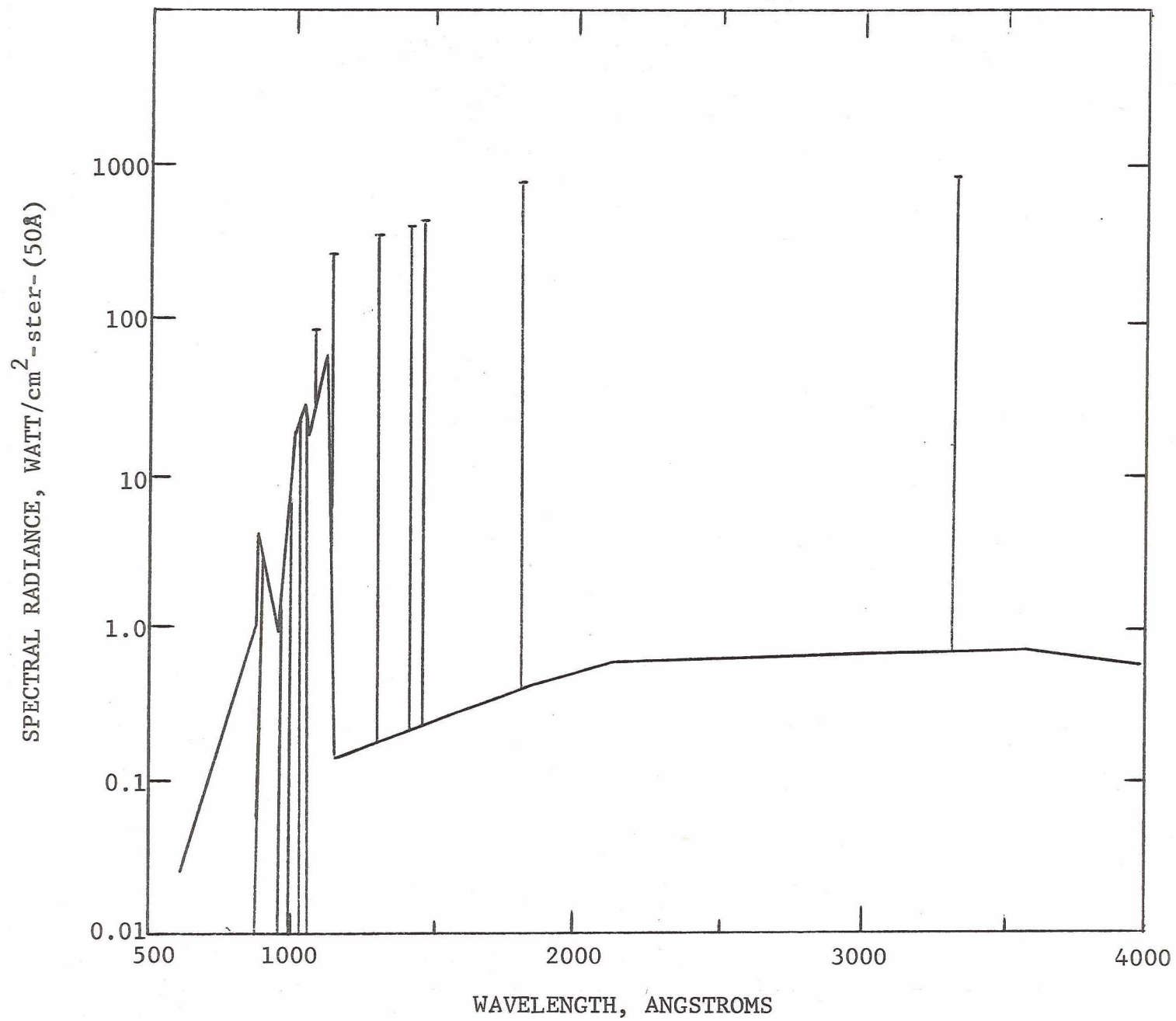


FIGURE 38. SPECTRAL RADIANCE AT BODY, NONADIABATIC CASE (9/18/69).

TABLE 9. SPECTRAL RADIATION AT DETECTOR PLANE
FOR EBERT SPECTROMETER DESIGN I.

NONADIABATIC CASE

<u>Wavelength</u>	<u>Power Incident On Detector</u>
600 Å	2.6×10^{-10} watt
1000	2.2×10^{-7}
2000	6.7×10^{-9}

ADIABATIC CASE

<u>Wavelength</u>	<u>Power Incident On Detector</u>
600 Å	5.1×10^{-8} watt
1000	2.0×10^{-6}
2000	2.0×10^{-8}

Reflectivity of each surface in the spectrometer is 5% and grating efficiency is 60%. Detector size is 0.45 x 2 mm.

The reflectivity of each surface was assumed to be 5%, giving a value of $T = 1.25 \times 10^{-4}$, and the efficiency of the grating was assumed to be $\epsilon = 0.60$. The noise equivalent power (NEP) of the detectors studied was presented in Table 3. This table is based on the use of a light chopper at the entrance slit and narrow band detector electronics giving a band width $\Delta f = 10$ Hz. A comparison of Table 3 and Table 9 enables the calculation of signal to noise ratios for the various detectors at the three different wavelengths. This S/N calculation is summarized in Table 10; it is evident that all detectors are of sufficient sensitivity. Associated electronics and recording systems must also be designed to handle a large dynamic range.

C. Other Spectrometer Designs

While the Ebert design appears feasible on the basis of flux considerations it is not the most efficient system possible since three reflections are required. Also, it must be remembered that the previous design considerations are based on the use of a chopper to modulate the radiation and a synchronous detection system. Should other modes of detection be desired the signal levels may have to be considerably increased.

TABLE 10. EXPECTED SIGNAL TO NOISE RATIOS FOR THE
DETECTORS FOR THE DESIGN I EBERT
SPECTROMETER. BANDWIDTH IS 10 Hz.

ADIABATIC						
WAVELENGTH	UDT-1	UDT-2	FPM-100	FPM-200	HPA-4204	SnO
500 Å	3.2×10^3	2.6×10^4	5.7×10^3	2.6×10^3	3.4×10^3	4.6×10^2
1000 Å	1.2×10^5	1.0×10^6	2.2×10^5	1.0×10^5	1.3×10^5	1.8×10^4
2000 Å	1.2×10^3	1.0×10^4	2.2×10^3	1.0×10^3	1.3×10^3	1.8×10^2

NONADIABATIC						
500 Å	1.6×10^1	1.3×10^2	2.8×10^1	1.3×10^1	1.7×10^1	2.3×10^0
1000 Å	1.4×10^4	1.1×10^5	2.5×10^4	1.1×10^4	1.5×10^4	2.0×10^3
2000 Å	4.2×10^2	3.4×10^3	7.4×10^2	3.4×10^2	4.4×10^2	6.1×10^1

Systems using a concave grating which require only one reflecting surface (the grating only) should be considered. A very simple system for use in the vacuum ultraviolet is the normal incidence spectrometer. In this design the slit is positioned so that the grating incidence angle is zero (i.e., normal incidence). The diffracted spectrum will lie on a circle whose diameter is the line joining the slit and grating. If such an instrument were to be constructed with the dispersion and resolution as that of the Ebert previously described, it would have a slit-to-grating distance of 150 mm and would occupy the same space as the Ebert. If a 20 x 20 mm grating is used the net gain over the Ebert design would be 400 times since the losses due to two reflections would be removed. The dispersion of the instrument would again be linear and an identical detector array could be used, if a 600 grove/mm grating is employed. If such a gain in flux is not required then the size of the grating can be reduced for the normal incidence instrument and a smaller volume could be achieved for the instrument.

Another possible design is the grazing incidence concave grating spectrometer. In this instrument very high incidence angles (70° to 80°) are used, with corresponding high angles of diffraction. The slit, grating, and spectrum all lie on a circle, tangent to the grating, with a diameter equal to the radius of curvature of the grating. Since the reflectivity at grazing incidence is very high the instrument is very efficient. A serious disadvantage, however, is the large non-linear dispersion. Non-linear dispersion is very undesirable in that each detector in the array of 30 would have to be of a different width. Astigmatism of the system is also very severe and the grating size is critical. For the present application, the grazing incidence instrument seems to offer no advantage over those systems described above.

IX. CONCLUSION

The solid state silicon photodetector can be used to obtain vacuum UV spectra over the 500 to 2000 Å region. The sensitivity, however, is not constant over this region and a minimum should be expected between 1000 and 2000 Å. The exact position and magnitude of the sensitivity reduction depends on the structure of detector. Among solid state detectors the surface barrier type devices should experience the least amount of sensitivity loss due to their thin absorption layer. Knowledge of the detector response over the spectral range of interest will permit accurate radiation measurements.

The surface barrier photodiodes were the most sensitive devices tested, with the diffused junction detectors lower by a factor of about 10. The noise equivalent power (NEP) for all the devices tested was approximately 10^{-11} watt at 1215.7Å.

The silicon areas immediately adjacent to the electrode on the surface barrier detectors, where the radiation did not have to penetrate the thin gold film electrode, appeared to be the most sensitive region and this fact must be considered when designing array detectors for the vacuum UV.

The most serious detector problem for actual employment in a spectrometer is the fatigue found in all the detectors but the Fairchild FPM 100 phototransistor. During experimental measurements the fatigue problem was most pronounced in the surface barrier devices, which had a fatigue period on the order of minutes. The recovery period was considerably longer, probably on the order of a day. The Fairchild photodiode had a decay period of about 20 seconds while the stannic oxide crystal did not exhibit a stable type of response and appears to be unacceptable as a spectrometer detector.

The fatigue effects might possibly be reduced by operation at higher bias voltages, or the detectors could possibly be prefatigued by subjecting them to some light radiation for a given period before measurements are to be obtained. The prefatiguing system might be a simple lamp in the spectrometer chamber that is activated for a pre-set period before spectrometer operation.

The phototransistor which did not fatigue appears to be the only immediately usable detector; however, its sensitivity in the 1400 to 2000 Å region was below the detection system threshold because of the low photon fluxes available. Consequently, no readings could be made over this region to determine the exact sensitivity values. Considering the response curves for the surface barrier detectors and the expected low transmission in silicon, a minimum in the phototransistor sensitivity curve is definitely expected in this region.

A high degree of crosstalk was exhibited by the United Detector Technology detectors which had more than one element on a single silicon wafer. Such crosstalk appears to be primarily associated with vacuum UV radiation which has a reduced penetration depth in silicon compared to visible light. One method of crosstalk reduction is to process the silicon so that the carrier lifetimes are reduced and to overcoat the regions between the elements so that definite opaque separations are present. An alternate solution is to use a series of discrete elements or devices such as the Fairchild detectors.

Solid state scanning of integrated arrays of silicon photodetectors has been investigated by a number of laboratories for use on cameras, character readers, and other image processing systems.¹⁴⁻¹⁹ It appears that if sufficient signal can be obtained the same techniques could be employed to scan the spectrometer detector array. The current problem is that synchronous detection is not compatible with the typical solid state array scanning system. Consequently, the signal must be above the low-frequency detector noise which requires that high signal levels compared to those obtained in the laboratory spectrometer used in this study must be present. This is one reason that the normal incidence type spectrometer design might be preferred over the Ebert type, since the photon fluxes are increased by the elimination of two reflecting surfaces.

Operation of the detectors in the photon flux integration mode should also realize higher signal outputs since the device is actively accumulating signal over the entire period between scans.²⁰ The principle of operation is that a p-n junction is reverse biased and then open circuited. The charge stored in the depletion layer capacitance then decays at a rate proportional to the incident radiation level. The charge required to periodically re-establish the initial voltage condition is monitored and provides a signal proportional to the incident radiation. When this mode of operation is used with phototransistors, gains of 1000 are possible.

Other operating factors such as long-term stability and environmental contamination appeared to be adequate. The frequency response of all the devices is in the micro-second or higher region and their dynamic range is reported to extend over 10 decades.²¹ Temperature effects are those normally experienced with silicon devices, and for the expected operating temperature the dark current and corresponding noise levels can be calculated. When operating with a grating system only the infrared and visible radiation scattered from the grating will be incident on the detector array so the heating will not be as great as a detector directly viewing the shock layer.

RECOMMENDATIONS FOR FUTURE WORK

1. Establish the sensitivity of the phototransistor and other diffused junction devices in the 1400 to 2000 Å region.
2. Determine the feasibility of operating detectors in the flux integration mode for solid state scanning and chopperless operation.
3. Investigate the reduction in detector fatigue by varying the bias voltage and operation with prefatiguing of detectors.

4. Explore methods of reducing the crosstalk on single-chip array detectors through shorter carrier lifetime devices.

5. Obtain and test large samples of the most desirable detector to assure consistent performance.

6. Measure the noise and analyze the operation of detectors in the d.c. mode of operation (no chopper in the system).

REFERENCES

1. R. L. Ohlhaber, M.P. Cann, and H. V. Watts, "Evaluation of Vacuum UV Detector-Systems for Capsule Reentry Measurements," NASA CR-1268, 1969.
2. E. M. Sullivan, W. D. Erickson, G. L. Smith, and J. T. Suttles, "Some Aspects of Interplanetary Earth-Entry Simulation," presented at the 15th meeting of the Institute of Environmental Sciences, Anaheim, California, April, 1969.
3. T. H. Slocumb, Jr. and R. W. Buchan, Private Communication, NASA, Langley Research Center.
4. R. G. Newburgh, L. Heroux, and H. E. Hinteregger, Appl. Opt. 1, 733, 1962.
5. R. E. Huffman, Y. Tanaka, and J. C. Larrabee, J. Opt. Soc. Am. 52, 857, 1962.
6. E. C. Bruner, Jr., J. Opt. Soc. Am. 59, 204, 1969.
7. E. E. Whiting, C. N. Burrous, and H. Sorensen, Appl. Optics 7, 2141, 1968.
8. M. L. Schultz and W. E. Harty, "Solid State Ultraviolet Photodetectors," AFAL-TR-68-112, RCA, June, 1968.
9. M. L. Schultz and W. E. Harty, "Solid State Ultraviolet Photodetectors," AFAL-TR-66-328, RCA, December, 1966.
10. A. J. Tuzzolino, Phys. Rev. 134, A205, 1964.
11. A. J. Tuzzolino, Rev. Sci. Inst. 35, 1332, 1964.
12. O. H. Schade, RCA, Rev. 9, 5, 1948.
13. G. Dearnaley and D. C. Northrop, "Semiconductor Counters for Nuclear Radiations," E. & F. N. Spon Ltd., London, p. 151, 1964.
14. P. K. Weimer, et. al., "Solid State Digital Scanning of Mosaic Sensors (Phase IV)," USAF, AFAL-TR-70-34, April, 1970.
15. R. A. Anders, et. al., IEEE Proc. of WESCON, 1967, paper 13/1, 1967.
16. G. P. Weckler and R. H. Dyck, IEEE Proc. of WESCON 1967, paper 13/2, 1967.
17. P. K. Weimer, et. al., IEEE Proc. of WESCON 1967, paper 13/3, 1967.
18. M. A. Shuster and W. F. List, Trans. of Met. Soc. of AIME 236, 375, 1966.
19. P. K. Weimer, Proc. IEEE 54, 354, 1966.
20. G. P. Weckler, Electronics 40, No. 9, 75, 1967.
21. R. L. Williams, "Fast High-Sensitivity Silicon Photo-diodes," J. Opt. Soc. Amer. 52, 1237, 1962.